Tumor cell-derived extracellular vesicles foster the immunosuppressive landscape of pancreatic cancer

Authors

Zainab Hussain[1*], Claudio Montenegro[2#], Christopher Rovera[1#], Djamila Belghoula[1], Sarah-Simha Tubiana[1], Pascal Finetti[1,3], Eugenie Lohmann[1], Magda Rodrigues[1], Thomas Bertran[1], Ghislain Bidaut[1], Daniel Isnardon[1], Sophie Vasseur[1], François Bertucci[1,3], Stephane Audebert[1], Luc Camoin[1], Moacyr Rego[2], Richard Tomasini[1*]

Affiliations

[1]Cancer Research Center of Marseille, Aix Marseille Univ, INSERM U1068, CNRS UMR7258, Institute Paoli-Calmettes, Marseille, France
[2]Therapeutic Innovation Center, Federal University of Pernambuco, Brazil
[3]Department of Medical Oncology, Institut Paoli-Calmettes, Marseille, France
[#] Contributed equally to this work
*Corresponding authors :
Zainab Hussain, Cancer Research Center of Marseille, 163 avenue de Luminy, parc scientifique de Luminy, 13288 Marseille Cedex 9, France, zainabhussain235@gmail.com, Tel : +33-4-91-82-88-15
Richard Tomasini, Cancer Research Center of Marseille, 163 avenue de Luminy, parc scientifique de Luminy, 13288 Marseille Cedex 9, France, richard.tomasini@inserm.fr, Tel : +33-4-91-82-88-15

Abstract

Pancreatic cancer remains a devastating disease with limited therapeutic options. Accumulating evidence show that cancer-associated fibroblasts (CAFs) and tumor-associated macrophages (TAMs), the predominant cells in the pancreatic cancer (PDAC) tumor microenvironment (TME), hinder anti-tumor immunity. However, the role of extracellular vesicles (EVs) in such process is poorly understood. In this study, using human bone-marrow-derived monocytes and PDAC tumor cells, we showed that tumor cell-derived EVs (TC-EVs) induced monocyte differentiation towards M2-like immunosuppressive $CD200R^{+}/PD\text{-}L1^{+}/HLA\text{-}DR^{-}$ macrophages that express ALOX15b, that we identify as an independent PDAC poor-prognosis biomarker using a human pancreatic cancer metacohort. We also demonstrated that TC-EVs reprogramed human primary PDAC CAFs, causing a fibronectin network reorganization associated with changes in extracellular matrix (ECM) composition, including alterations of the WNT pathway elements such as SFRP1 enrichment. We further revealed that monocytes cultured on rSFRP1-enriched ECM differentiated also into M2-like immunosuppressive macrophages. Lastly, we demonstrated that both directly and indirectly TC-EVs, or rSFRP1-enriched ECM, driven differentiated macrophages hindered T-cell activation and subsequent anti-tumor activity. Our findings highlight novel, dual mechanisms of TC-EVs-mediated crosstalk, involving $ALOX15b^{+}$-Macrophages and $SFRP1^{+}$-CAFs, that simultaneously contribute to foster the immunosuppressive ecosystem of pancreatic cancer.

The authors have declared that no conflict of interest exists.

Introduction

Pancreatic cancer (PDAC) is a devastating and fatal cancer, expected to be the third-leading cause of cancer-related deaths by 2030 in developed countries (1). These dismal characteristics are largely attributed to late diagnosis mostly established at advanced stages coupled with a lack of efficient therapies, mainly focused on targeting tumor cells. The only curative therapy for PDAC is surgical resection, for which merely 20% of patients are eligible. The majority of patients are consequently subject to systemic chemotherapies, with rapidly acquired resistance, and/or palliative care (2). The recent breakthrough of immunotherapies, aiming to prime and reactivate the patient's natural defenses against the tumor, primarily through immune checkpoint inhibitors (ICI), has revolutionized cancer care in many solid cancers such as melanoma, non-small-cell lung cancer and colorectal cancer, among others. Unfortunately, the remarkable efficacy of these therapies has not translated to PDAC (3). Thus, there are critical needs to understand the immune environment of PDAC and to develop new therapeutic avenues to improve PDAC patients' fate and management.

Indeed, PDAC is distinct from other solid tumors due to the presence of a highly dense, prominent, fibrotic and immunosuppressive tumor microenvironment (TME), often accounting for the majority of the tumor bulk. This heterogeneous TME is predominated by various subtypes of constitutively activated fibroblasts, known as cancer-associated fibroblasts (CAFs), responsible for the deposition of the dense extracellular matrix (ECM) that acts as a barrier to diffusion of therapies and to the infiltration of anti-tumoral immune cells (4, 5). Tumor-associated macrophages (TAMs), highly immunosuppressive, anti-inflammatory innate immune cells, represent the second main cellular component of PDAC TME (6). The immunosuppressive ecosystem orchestrated by the components of the TME results in exclusion or inactivity of anti-tumoral immune cells, such as T-cells, and protects tumor cells from immune attack through antigen-presentation deficiency and induction of immune tolerance. Thus, PDAC is notoriously categorized as an "immune cold" cancer type, deserted of active cytotoxic immune cells, which in part may explain the failure of immunotherapies (3, 7).

Interactions between the tumor compartment and the TME has become a pronounced subject of interest in tumor biology, as we now recognize that the extensive and dynamic crosstalk between these two compartments can modulate, among others, tumor progression and anti-tumor immunity. Signals derived from tumor cells were found to activate resident pancreatic stellate cells to CAFs, leading to ECM remodeling, and sustained CAF reprogramming to create feedback loops facilitating tumor progression (8–10). Tumor-TME communication has also been reported to recruit and maintain immunosuppressive myeloid cells, and tolerance-inducing regulatory T-cells, hindering therapeutic responses (11, 12). Cell-cell communication may occur through direct contact, secretion of soluble factors, as well as of extracellular vesicles (EVs). EVs are nano- to micro-meter-sized cellular representations, secreted by all cell types, diffusing into tissues and bodily fluids, and capable of traveling away from their cells of origin (13). EVs, recognized as prominent mediators of intercellular communication, contain a large variety of cargo, including lipids, nucleic acids, and proteins, and are found to be secreted in high quantities by tumor cells. Particularly, PDAC tumor cell-derived EVs (TC-EVs) were found to regulate hepatic pre-metastatic niche formation, induce angiogenesis in hypoxic conditions, inhibit natural killer cell function, and confer chemoresistance, together contributing to tumor progression and metastasis (14–18).

Despite the fact that TC-EVs are highly heterogeneous and contain many layers of information, their role in the dynamic and concomitant modulation of the PDAC TME remains elusive. Accordingly, we sought to characterize the phenotypical and functional impact of PDAC TC-EVs on the formation of a pro-tumoral and immunosuppressive microenvironment by studying their effects on the modulation of two major components of the TME, monocytes, as the major precursors of TAMs, as well as CAFs and its subsequent production of the ECM. We modelled

the proximal impact of TC-EVs on macrophage trafficking by studying the differentiation of bone-marrow derived monocytes. In parallel, we investigated the impact of TC-EVs on CAFs-derived ECM and revealed the consequent influence of this modified ECM on monocytes differentiation, highlighting a distal function of TC-EVs to foster an immunosuppressive TME. Through this study, we demonstrated that TC-EVs mediate a complex cross-communication between TME cell types. TC-EVs directly differentiate infiltrating monocytes to TAM-like, immunosuppressive macrophages and this phenotype is mirrored with monocytes cultured on ECMs produced by TC-EVs-treated CAF, providing two avenues of TC-EVs-mediated immunosuppression, as both resulting in T-cell inactivation evidenced by their reduced proliferation, expression of activation markers, and cytotoxic potential against tumor cells. Overall, our study highlights novel dual mechanisms of TC-EVs-mediated immunosuppression in the PDAC TME, highlighting markers of immunosuppressive CAF-ECMs as well as of TC-EVs differentiated macrophages that could be potential combinatory targets or biomarkers to improve therapeutic outcomes in PDAC.

Results

PDAC TC-EVs drive direct healthy monocytes differentiation into M2-like macrophages. The direct impact of TC-EVs on freshly-isolated healthy monocytes differentiation and resulting phenotype was investigated 5 days following treatment as depicted in Figure 1a. First, cells-derived EVs were isolated by combining differential ultracentrifugation and size-exclusion chromatography (Figure S1A), their morphologies and particle sizes/concentrations were investigated by NTA (Figure S1B-D) and electronic microscopy (Figure S1E). Moreover, expression of common EV-markers was assessed by Western Blot (Figure S1F). Uptake of TC_1 (PANC-1)-released EVs (TC_1-EVs) by monocytes resulted in increased granularity as evidenced by higher side scatter (Figure 1b). Internalization of TC_1-EVs by monocytes was confirmed using general lipid-membrane green labeling dye PKH67 labelled TC_1-EVs incubated with monocytes for 24 hours followed by flow cytometry analysis. On average, 60% of the total cell population had internalized EVs following 24h of incubation (Figure 1c). Cell viability of monocytes treated with TC_1-EVs was assessed by annexin-V/propidium iodide (PI) staining (Figure 1d-e and S1G) at 96 hours after TC_1-EVs addition and by Incucyte live-cell imaging using cytox-green dead-cell marking agent uptake at 72 hours after TC_1-EVs addition (Figure 1f-g). Each technical approach revealed an improvement of cell viability in TC_1-EVs-treated monocytes.

Then, we investigated the differentiation of freshly isolated healthy blood-donor derived monocytes following 5 days treatment with various stimuli including: human pancreatic tumor cells-derived EVs such as PANC-1-released EVs (TC_1-EVs) and MiaPaCa-2-released EVs (TC_2-EVs) and non-tumoral human pancreatic epithelial ductal cells (HPDE)-released EVs (HPDE-EVs), their respective supernatants (SN)-depleted of EVs, as well as DMEM and K-SFM medium-derived EVs and their respective SN-depleted of EVs, and M-CSF as a positive control following the experimental procedure described in Figure 1a. Resulting differentiated macrophages were analyzed by flow cytometry for the percentage of cells of the total population expressing monocyte, macrophage and antigen-presenting cell markers (Figure 2a, Figures S2A, S3A and C), and their median fluorescence intensities (Figure 2b, Figures S2B, S3B and D). Compared to the untreated condition, treatments with TC_1- or TC_2-EVs resulted in a marked increased percentage of total cell populations expressing M2-macrophage markers CD206/CD200R and immune checkpoint ligand PD-L1 (Figure 2a, Figure S2A) while mean fluorescence intensity (MFI) of HLA-DR was reduced by TC_1- and TC_2-EVs (Figure 2b, Figure S2B). Interestingly, while some of those modified expression patterns (either in percentage or MFI) were also observed using control conditions involving conditioned medium depleted of EVs confirming that secreted elements from pancreatic tumor cells induced monocytes differentiation, the modified expression patterns of CD200R and PD-L1 were specific to TC_1 or TC_2-EVs (Figure S3A-D). Altogether those data reveal that pancreatic TC-EVs treated monocytes differentiated towards a $CD200R^{+}/PD\text{-}L1^{+}/HLA\text{-}DR^{lo}$ macrophage phenotype.

The secretory profile of monocytes treated with TC-EVs was analyzed by multiplex ELISA (Luminex) of 32 relevant chemokines and cytokines in the conditioned medium of control (untreated) and TC_1-EVs differentiated macrophages. Globally, an overall increase in chemokine and cytokine production was observed (Figure 2c). Specifically, we could detect a marked increase of M2-macrophages related chemokines/cytokines such as monocyte chemoattractive protein-1 (MCP-1)/CCL2, interleukin-1 receptor antagonist (IL-1RA), stromal cell-derived factor-1α (SDF-1α), B lymphocyte chemoattractant (BCL)/CXCL13, IL-15, and IL-21 in TC_1-EVs differentiated macrophage conditioned medium (Figure 2d). At the physiological level, one of the functional characteristics of M2-macrophages is phagocytosis. Thus, the phagocytic capacity of untreated and TC_1-EVs treated macrophages was investigated by their incubation with green-fluorescent E. coli bioparticles following their differentiation period. Although donor-based variability in amplitude of phagocytosis was observed, TC_1-EVs differentiated macrophages showed a substantial increase in phagocytosis compared to untreated macrophages over a 16-hour period (Figure 2e, Figure S2C). Altogether, our result

reveal that PDAC TC-EVs lead monocytes differentiation towards physiologically active M2-like macrophage.

PDAC TC-EVs-differentiated macrophages reduce T-cell activation and cytotoxic activity towards tumor cells. Since TC-EVs differentiated macrophages demonstrated an M2-like phenotype, which is known to correlates with immunosuppressive abilities (19), we evaluated their functional impact on T-cells activity/activation. Following the previous protocol, the differentiated macrophages were co-cultivated for 72-hours with same-donor activated T-cells at a 1:1 ratio as depicted in Figure 3a. First, we analyzed their proliferative activity using the Cell-trace violet assay and observed that while activated T-cells from co-culture with untreated macrophages showed reduced normalized mean CFSE fluorescent intensity reflecting an increase in T-cells proliferation and thus their increased activation, activated T-cells from the same donors in co-culture with TC_1-EVs differentiated macrophages showed a decreased proliferation as shown by higher normalized mean CFSE fluorescent intensity (Figure 3b, figure S4A). In agreement with this T-cell proliferation, we show that expression of T-cell activation markers CD25 and CD69, and co-stimulatory factor CD28, was decreased in activated T-cells co-cultured with TC-EVs differentiated macrophages compared to those co-cultured with untreated macrophages (Figure 3c). Finally, to analyze whether these T-cells, with reduced proliferation/expression of activation markers, had a modulated cytotoxic potential, we implemented the previous protocol (Figure 3a) with final co-culture with either TC_1 or TC_2, depending the TC-EVs used to induced monocyte differentiation, to evaluate their tumor-cell killing ability (Figure 3d). Through live-imaging of co-cultures and incubation with Incucyte caspase 3/7 reagent, both TC_1 and TC_2 revealed reduced levels of caspase 3/7 staining when cultivated with T-cells from their respective TC-EVs differentiated macrophages co-cultures compared to co-cultures with untreated macrophages (Figure 3e-f). Similarly, cumulated percentages of cells positive for annexin-V^+, PI^+ and double positive annexin-V^+/PI^+TC were reduced when co-cultivated with T-cells from their respective TC-EVs differentiated macrophages co-cultures compared to T-cells from untreated macrophage co-cultures (Figure 3g-h, Figure S4B), indicative of reduced TC death and T-cell cytotoxic potential. Overall, those results demonstrate that TC-EVs differentiated macrophages drive a reduced proliferation, activation, and cytotoxic activity of T-cells.

PDAC TC-EVs differentiated macrophages highlight a distinct protein signature. We then investigated the proteomic profile of TC-EVs differentiated macrophages to establish a TC-EV correlated specific signature of these macrophages. We prepared 3 biological independent experiments of TC_1, TC_2 and non-tumoral pancreatic ductal cell (HPDE) EVs-differentiated macrophages (from 3 independent blood donors), for proteomic analysis by mass spectrometry (MS), following the same treatment design as in Figure 1a. As HPDE-EVs were not able to induce the M2-like differentiation of monocytes observed following TC-EVs treatments and specifically highlighting a CD200R^+/PD-$L1^+$/HLA-DR^{lo} phenotype (Figure 2a-b, Figure S3A-B), we considered that significantly dysregulated proteins following HPDE-EVs treatments (Figure 4a, figure S5A) could not be part of our specific signature of interest, nor responsible for monocytes differentiation, and, consequently, we removed those proteins from our following investigations. The non-specific TC-EVs impact on monocytes protein content was accounted for by non-considering differentially expressed proteins in monocytes treated by non-tumoral pancreatic ductal cell-derived EVs (HPDE-EVs) (Figure 4a, figure S5A).

To account for donor variability, proteins that were differentially expressed in 2 out of 3 donors were considered. Thus, we were able to highlight 109 and 54 differentially expressed proteins in macrophages specifically treated with TC_1- and TC_2-EVs respectively (Figure 4a-c, figure S5A-C). Pathway enrichment analysis revealed enrichment of proteins primarily in cytoplasmic large ribosome constituent, blood coagulation/healing, anchoring cell-substrate junction adhesion, phagocytosis, and secretory actomyosin granules in TC_1-EVs differentiated macrophages (Figure 4d) and in cytoplasmic large ribosomal subunit, anchoring cell-substrate focal junction, initiation factor granule, and polysome ribosomes in TC_2-EVs differentiated macrophages (figure S5D). The use of STRING analysis to denote protein interactions, with

Markov-cluster algorithm (MCL) clustering, revealing 22 and 10 clusters in TC_1- and TC_2-EVs differentiated macrophages respectively (Figure 4e and S5E) and the enriched pathways interactions were summarized in a radial plot for the TC_1- and TC_2-EVs differentiated macrophage respectively (Figure S5F and S5G). Interestingly, only 12 commonly differentially expressed proteins were found between TC_1- and TC_2-EVs differentiated macrophages, representing a specific protein signature of macrophages differentiation driven by TC-EVs (Table 3).

Alox15B from the signature of PDAC TC-EVs differentiated macrophages correlates with poor prognosis. We interrogated the clinical relevance of the expression of each gene coding for those 12 proteins by correlating their relative mRNA expression with clinical characteristics in a large PDAC cohort (Table 2). A total of 1248 samples were analyzed including 158 normal pancreas, 938 primary tumors, and 152 metastasis samples. The expression pattern of the 12 members of the signature revealed significant modulations in correlation with the origin of tumor samples (Figure 5a and S6A-C). Among those 12 markers, we focused our attention on *ALOX15B* as its high expression correlated with the basal-like PDAC subtype which is a poor-prognosis sub-type (Figure 5b), and *ALOX15B* expression was the only significant poor-prognosis marker for overall survival (OS) and disease-free survival (DFS) in the whole cohort of primary tumors (Figure 5c-d and S6D-E). The patients with high expression showed 32% 5-year OS (95%CI 27-37) and 28% 5-year DFS (95%CI 23-33) *versus* 44% (95%CI 39-50) and 39% 5-year DFS (95%CI 34-44) respectively for those with low expression. Interestingly, high *ALOX15B* expression retained its poor-prognosis value in multivariate analysis for both DFS and OS (data not shown), suggesting independent prognostic value from the Moffitt's molecular subtypes notably. High *ALOX15B* expression was associated with lower DFS and OS in both Moffitt' subtypes (Figure 5e-f). We further validated the expression of *ALOX15B* in macrophages using our clinical cohort of PDAC bulk transcriptomes (Figure S6F) as well as single cell RNA sequencing public datasets (Figure 5g) and even more specifically in M2 macrophages using some major M2 markers such as *CD206*, *CD163* or *CD209* (Figures 5h and Table 4) and M1 markers such as *CD83* and *CD74* (Figure S6G and Table 4). Finally, we compared the prognostic information for OS provided by *ALOX15B* expression alone, by the Bindea's macrophage score alone, and the combination of both. The macrophage score displayed prognostic value with shorter OS associated with higher score (Figure 5i). Given this observation and the prognostic value of *ALOX15B* expression, and given the correlation between both variables, we searched for an eventual prognostic value of a model combining both of them. As shown in Figure 5i, this model was prognostic, with longer OS in patients with both low *ALOX15B* expression and low macrophage score than in patients with non-low/low profile. Interestingly, the combined model provided more prognostic information than each variable separately (Figure 5j and S6H), and each variable significantly contributed to enhance the prognostic value of the other one ($p<0.05$ for the two ΔLRX2). Altogether these data demonstrate that among the specific protein signature of M2-like macrophages differentiation driven by TC-EVs, the expression of *ALOX15B* correlates with poor prognosis and more aggressive tumors in PDAC patients, independently from classical prognostic features.

PDAC TC-EVs influence primary cancer associated fibroblasts structuration of fibronectin fibers. We then investigated the indirect impact of TC-EVs on freshly-isolated healthy monocytes differentiation. As PDAC associated immune cells are evolving within a dense extra-cellular matrix (ECM) network we hypothesized that TC-EVs could influence monocytes differentiation through a modulation of the cancer-associated fibroblasts (CAFs)-derived ECM. We first evaluated the impact of TC-EVs on CAF-produced ECMs using two different PDAC patients' primary CAFs, treated with TC_1- or TC_2-EVs during an 8-day incubation period required for cell-derived ECM production (Figure 6a). At the end of the 8-day period, ECMs were decellularized and analyzed by immunofluorescence for fibronectin fiber structural characterization. Confocal microscopy images show less uniform directionality as well as less dense and more porous fibronectin fibers in the TC-EVs treated CAF conditions

compared to controls (Figure 6b). Structural features of these fibronectin fibers were quantified using the ImageJ plugin TWOMBLI (The Workflow Of Matrix BioLogy Informatic), a pipeline allowing for the quantification of various features (matrix fiber alignment, endpoints). Interestingly, quantification of fiber alignment showed lower alignment of fibronectin fibers in the TC-EVs treated condition for one type of primary CAF (Figure 6c) while the number of normalized fiber endpoints per unit length was increased in TC-EVs treated condition for the other primary CAF (Figure 6d). Quantification of other TWOMBLI parameters such as lacunarity, fiber length, branchpoints, curvature, hyphal growth unit (HGU) and fractal dimension, were also significantly different between both primary CAF-derived ECM but always under dependency of TC-EVs treatment (Figure S7A-B). Interestingly, ECM produced by CAF treated with HPDE-EVs do not recapitulate structural features modification such as matrix fiber alignment (Figure S8A-B). Those data reveal that, while reflecting CAFs heterogeneity among PDAC patients, TC-EVs are able to specifically modulate the CAFs-derived Fibronectin structuration.

ECM produced by PDAC TC-EVs treated CAFs favor PDAC tumor cells aggressiveness. To assess the biological relevance, in correlation with PDAC aggressiveness, of TC-EVs treated CAF-derived ECMs, TC_1 and TC_2 were plated on untreated or their corresponding TC_1/TC_2-EVs treated CAF-derived ECMs then we evaluated their migratory and invasion abilities (Figure 6e). We observed that TC_1 and TC_2 cells showed improved migratory capacities, through time-lapse microscopy over a 12-hours period (Figure 6f and S8C)). Specifically, total migration distance of each tumor cell type was increased where speed and total displacement were not significantly impacted by plating on EV-treated CAF-ECMs (Figure S7C-D). We further observed that both TC_1- and TC_2- cells invaded more through their respective EVs-treated CAF-derived ECMs than control ECMs (Figure 6g, figure S7E-H). Thus, TC-EVs treated CAFs produce a pro-tumoral ECM favoring pancreatic tumor cells aggressiveness.

PDAC TC EVs-treated CAFs produce ECMs with increased expression of Wnt pathway proteins SFRP1 and Wnt5a. To investigate how TC-EVs may modify the composition of the ECM deposited by CAFs, and whether the potentially modified composition contributes to the increased aggressiveness of tumor cells, we performed the proteomics evaluation of CAF-ECMs (matrisome), using control ECM or ECM treated with TC_1-EVs by mass spectrometry (LC-MS/MS). Heat map and volcano plots show 76 differentially expressed proteins in TC_1-EVs-treated CAF-derived ECM (p-value < 0.05, $\log_2$-fold change $<$ or > 0.5) (Figure 7a-b). Through gene enrichment analyses, differentially expressed proteins found in the TC_1-EVs treated CAF-ECM group were found to be primarily enriched in regulation of transmembrane receptor protein serine/threonine kinase signaling pathway and transforming growth factor beta receptor superfamily signaling pathway among others (Figure 7c). By combining those differential analyses, we focused our attention on the GO term "Wnt signaling pathway" (enrichment score of 0.705; *p*-value of 0.0001) which involves the most enriched protein, secreted frizzled related protein-1 (SFRP1) with a Log-2-fold change of 4.46 (Figure 7b). In line with our hypothesis, recent evidences suggest $SFRP1^+$-CAFs as modulator of the immune ecosystem (20). Using KEGG we could reveal the WNT protein cluster and highlight SFRP1 as the unique upregulated protein in TC1-EVs treated CAFs ECM linking the 3 Wnt pathways present in the analysis (Figure 7d). STRING analyses confirmed such clustering with a Wnt protein cluster with SFRP1 as a core central linking protein (Figure 7e). Therefore, the ECM produced by CAFs following TC-EVs treatment revealed marked modification in protein content such as WNT elements and notably an enrichment in SFRP1.

SFRP1 in TC-EVs treated CAF derived ECM favor monocytes to macrophage differentiation to reduce T-cell anti-tumoral activity. We validated our matrisome findings using PDAC patient samples and investigated for SFRP1 level in healthy pancreas, PDAC tissue samples and publicly available datasets of PDAC patient cohort. We observed that SFRP1 level was only detected in PDAC samples (Figure 8a) with a specific staining detected in non-tumor cells along with its expression in the tumoral compartment (Figure 8a). CAFs

being the main ECM producer in PDAC, we searched for CAF expression of SFRP1. Using single cell RNA sequencing from publicly available datasets, our investigation revealed that *SFRP1* is indeed expressed in CAFs (Figure 8b-c). More specifically, we could determine that *SFRP1* is expressed by a specific subset of CAFs, the inflammatory CAFs (iCAFs), as shown by a strong correlation with known major iCAFs markers such as C3, C7, CFD, PTGDS or CXCL12 (Figure 8d and Table 5). In parallel, we could reveal that *SFRP1* expression in CAFs do not correlate with myofibroblast (myCAF) markers, *MMP11* and periostin (Figure 8b and S9A), and do not co-localize with αSMA, a master myCAF marker (Figure S9B). Interestingly, *SFRP1*$^{+}$-CAFs highly correlate with *IGF1*$^{+}$-CAFs (Figure 8d), described as an early activated state that represent the predominant iCAF described in PDAC in the current literature, and differ from *IL11*$^{+}$-iCAFs that correlate with inflammatory monocytes infiltration in PDAC (21). We further assessed the clinical relevance of *SFRP1* expression in human PDAC by analyzing mRNA expression levels in the 1248 samples of our gene expression database. *SFRP1* expression was variable according to the sample's origin (Figure 8e). We defined high and low expression groups based on median *SFRP1* mRNA expression. We showed that *SFRP1*-high PDAC patients were associated with an increased EMT Metagene score, an increased Bindea macrophage score as well as with the squamous subtype in Bailey's classification, the quasi-mesenchymal subtype in Collisson's classification and the basal-like subtype on Moffitt's classification, which represent the subtypes with worst overall survival (22)(Table 6).

Since both *SFRP1*$^{+}$-CAFs and iCAFs (correlating with *SFRP1* expression) have been described as modulators of tumoral immune response (21, 23) (Figure S9C-E), we decided to evaluate their impact on monocytes differentiation as compared to the direct impact of TC-EVs on monocytic differentiation previously described (Figures 1-5). Monocytes were extracted from healthy human blood donors as previously described and plated on decellularized CAF-derived ECMs, untreated, treated with TC_1-EVs, or TC_2-EVs, or supplemented with rSFRP1 (Figure 8f). After 5 days culture on ECM, following immunophenotyping using flow cytometry we observed that monocytes plated on TC_1- or TC_2-treated CAF derived ECMs and rSFRP1-supplemented CAF-derived ECM showed an increased frequency of positive population expressing M2 macrophage markers CD200R (Figure 8G). This evidence is in line with the positive correlation we observed between *CD163*$^{+}$-Macrophages and *IGF1*$^{+}$-iCAF (Figure S9F and G). After 5 days of monocytes culture on ECM, same donor activated T-cells were added for 72 hours before being extracted for cocultures with TCs for cytotoxicity analysis using Annexin-V/PI staining of TCs and evaluated after 24 hours (Figure 8h). We observed that T-cells from TC_1-EVs treated CAF-derived ECMs and rSFRP1-supplemented CAF-derived ECMs had reduced cytotoxic potential against pancreatic tumor cells indicative of a decreased activation state of T-cells (Figure 8i). Overall, our data demonstrate that tumor cell derived EVs drive CAFs reprogramming to produce an SFRP1-enriched ECM that consequently impact monocyte-to-macrophage polarization and T-cell activity, fostering the development of an immunosuppressive ecosystem.

Discussion

Pancreatic cancer remains one of the most lethal malignances, distinguished by a grim prognosis with a 5-year survival rate which barely reaches 10 to 12%. Even with the emergence of more efficient chemotherapeutic regimens such as FOLFIRINOX, PDAC patients' survival was merely increased of few months in the last 20 years (24). While numerous solid tumors showed important progress in patient survival notably due to the rise of immunotherapies, no improvements have been reported thus far for PDAC patients. Immune checkpoint inhibitor therapies are efficient for less than 1% of PDAC patients. This failure is imputed to the specific and prevalent nature of the intra-tumoral microenvironment of these tumors that is considered as highly fibrotic and immunologically "cold". While immune cells of the TME have already been reported as key actors of immunotherapy resistance (25), the TME of PDAC is mostly infiltrated with immunosuppressive cells such as Tregs, MDSCs and TAMs, which contribute to immune evasion and resistance to immunotherapies (26). The PDAC TME is further characterized by a deficiency in adaptive T-cell immunity, with the absence of effector T-cells, explaining the tumor's disability to further respond to immune checkpoint inhibitors. Thus, understanding the immune ecosystem of PDAC and the relationship established by immune cells with other PDAC cell components is critical to optimize available immunotherapies or even further develop emerging immunotherapies strategies.

Intercellular communication between PDAC tumor cells and components of the TME is essential in regulating tumor progression by activation of CAFs and formation of the desmoplastic reaction, hinderance of immune surveillance, angiogenesis, and resistance to chemotherapies (27, 28). EVs are prominent mediators of this communication, capable of systemic circulation, diffusing at great distances from their various cells of origin while carrying simultaneously multiple cargo with various methods in transmission of their information, multiplying their communicative potential (29). These unique characteristics of EVs highlight them as intriguing actors of tumor-driven immune evasion and tumor progression yet remain largely unexplored in PDAC. Here, we demonstrated that tumor cell-derived EVs are key modulators of two main cellular actors within the PDAC TME, namely CAFs and macrophages, in order to foster an immunosuppressive ecosystem. Tumor-cell derived EVs are capable (i) to directly differentiate monocytes to M2-like immunosuppressive macrophages with a unique protein expression profile with ALOX15b as associated marker, and (ii) to indirectly favor the formation of M2-like macrophages through the formation of a specifically SFRP1-enriched extracellular matrix produced by CAFs. Together, both paths of macrophage differentiation led to T-cell inactivation and reduction of their cytotoxic potential. These findings highlight novel mechanisms of monocyte-derived macrophage differentiation simultaneously at proximal and distal levels, with tumor cell EVs at its core, supporting immune evasion and tumor aggressiveness in PDAC.

High levels of circulating and recruited monocytes in PDAC has been found to be linked to poor prognosis, tumor progression, and immune checkpoint blockade (30–32). Monocytes are the most prominent source of TAMs compared to embryonic-origin macrophages and play a key role in antigen presentation and thus immune escape and tumor growth (33, 34). As tumor-derived EVs and monocytes both circulate systemically in blood and these EVs can be in contact with tumor-infiltrating monocytes, we hypothesized that TC-EVs can influence monocyte-to-macrophage differentiation locally or at distance, and consequently support immune evasion. Our findings confirmed the internalization of tumor-derived EVs by monocytes, which was recently found to be mediated by transmembrane protein CD44H on monocytes and resulted in activation of the STAT3 pathway (35). Interestingly, we have demonstrated increased survival and direct differentiation of healthy monocytes into alternatively-activated M2/TAM-like immunosuppressive macrophages by EVs generated from 2 different PDAC tumor cells, without the need for classical differentiation cytokines such as M-CSF. Classical monocytes normally circulate for one day in blood in steady states (36). It was previously found that EVs derived from lung, breast, and hepatocellular carcinoma cells supported monocyte survival in line with our findings (37). To be an active source of TAMs in

the TME and to continually support immunosuppression, TC-EVs in PDAC may thus promote monocyte survival and subsequent infiltration and attraction into tumor tissues. Analysis of monocyte/macrophage marker expression allowed us to demonstrate variable expression of markers in TC_1- and TC_2-EVs treated monocytes, firstly denoting the heterogenous action of different tumor cell line-derived EVs on monocyte differentiation. Nonetheless, a consistent increase of well-established M2-macrophage marker, CD200 Receptor 1, associated with phagocytosis and poor prognosis in PDAC (38), was observed in both TC_1- and TC_2-EVs treated monocytes. Immune checkpoints, against which immunotherapies are targeted, control T-cell activation and responses and are largely manipulated by tumors to evade the immune response in multiple cancers. Here, we demonstrated that TC_1- and TC_2-EVs, but not M-CSF, were capable of inducing higher expression of the immune checkpoint ligand PD-L1 demonstrating an EV-induced immunosuppressive characteristic of macrophages in PDAC. Clinical correlation analyses of the proteomic signature from TC-EVs differentiated macrophages we highlighted allowed for the identification of arachidonate 15-lipoxygenase type II (15-LOX2), encoded by the gene *ALOX15B*, as upregulated in TC-EVs differentiated macrophages in correlation with increased metastases and poor disease-free and overall survivals. 15-LOX2, conversion of polyunsaturated fatty acids to hydroxy fatty acids, is constitutively expressed in human monocyte-derived macrophages and related to efferocytosis and ferroptosis. Expression of 15-LOX2 specifically by TAMs can result in an increase of bioactive lipid molecules in the TME and contribute to tumorigenesis as well as modify macrophage functions in relation to anti-tumoral immunity. IL-13 induced macrophages were associated with 15-LOX2 expression, as part of a leukotriene synthesis related M2 signature, as well as T-cell dysfunction, immune checkpoint expression, and unfavorable outcomes in glioma and had high CCL2 secretion in renal cell carcinoma (39, 40). In line with the above findings, we demonstrated the high expression of 15-LOX2 in PDAC TC-EVs differentiated macrophages, associated with $CD200R^{+}$/$PD\text{-}L1^{+}$/$HLA\text{-}DR^{lo}$ expression, immunosuppressive cytokine and chemokine secretion, impedance of T-cell activation, and correlating with poor patient outcome. Future studies investigating the mechanistic regulation of 15-LOX2 increase in macrophages, following TC-EVs, could shed lights on potential new target to control macrophage-to-lymphocyte interactions resulting in immunosuppression.

Under the influence of tumor-derived signals, TAMs secrete cytokines and chemokines promoting tumor growth, metastases and mediating immune suppression (41–43). Among the secreted factors analyzed, TC-EVs differentiated macrophages showed the highest expression of MCP-1/CCL2 and IL-1RA and increased secretion of SDF1a, CXCL13, IL-1RA, IL-15, and IL-21 compared to untreated macrophages. The CCL2/CCR2 axis has been widely implicated in recruitment of monocytes resulting in activation of TAMs and MDSCs, thus regulating immune checkpoint blockade (44–48). In addition, SDF-1a or CXCL12 is also a potent chemoattractant of monocytes resulting in TAMs and contributing to T-cell exclusion in PDAC (49). Increased secretion of CCL2 and SDF1a/CXCL12 by TC-EVs macrophages could thus represent an imperative source of these chemokines in the PDAC TME, potentially regulating a positive-feedback loop of monocyte tumor infiltration and subsequent immunosuppressive TAM formation. Our study further highlighted several cytokines and chemokines that can be pro- or anti-tumoral (IL-1RA, IL-15, IL-21, CXCL-13) demonstrating the need to further investigate their role in tumor progression and immune escape, in PDAC, in concertation with other secreted factors.

The PDAC immune TME is marked by low levels of effector T cells, an effect largely mediated by immunosuppressive macrophages (50). The M2-like, immunosuppressive phenotype of TC-EVs differentiated macrophages was functionally validated by their impact on T-cell proliferation, activation, and anti-tumor cytotoxicity. Furthermore, these T-cells had consistently decreased expression of activation markers CD25 and CD69 as well as co-stimulation marker CD28, essential for effector T-cell activity. Consequently, we demonstrated that T-cells in contact with TC-EVs differentiated macrophages are not efficient in killing tumor

cells, the same ones that were a source of EVs, highlighting a novel mechanism of reduced anti-tumoral immunity in PDAC via EVs.

In addition to directly influencing infiltrating monocytes, tumor cell-derived EVs can contact CAFs within the TME and modulate their desmoplastic activity, consequently influencing tumor cells and infiltrating immune cells. Thus, we characterized the ECM produced by CAFs under influence of TC-EVs and its resulting impact on tumor cell activities as well as monocyte phenotypes and differentiation to macrophages. One of the major components of the ECM is fibronectin, a scaffolding and signaling protein found to be highly expressed in PDAC tumor stroma, is associated with larger tumors and advanced disease, and required for assembly of other ECM proteins and collagens (51–53), impacting as well the migration of tumor cells away from the primary tumor site and the establishment of pre-metastatic niches in the liver respectively (14, 54). Our present study shows that TC-EVs reduced fibronectin alignment and increased branching in specific patient CAF-derived ECMs, potentially indicative of tumor-EVs mediated fibronectin remodeling depending on CAF type.

Although fibronectin structural modifications were not consistent between primary CAF samples in our study, all TC-EVs treated CAF-derived ECMs resulted in increased migration and invasion of tumor cells suggesting that factors other than structure were at play in maintaining pro-tumoral aspects of the CAF-derived ECM (55–57). Thus, we evaluated ECM composition following treatment of CAFs with TC-EVs and revealed that TC_1- and TC_2-EVs differentially modified CAF matrisome profiles, demonstrating an heterogeneity in the impact of tumor-EVs, potentially due to their modified content. Among pathways and processes highlighted we noticed the presence of members of the WNT pathway, notably SFRP1, not transferred directly from TC-EVs and thus likely produced by CAFs through induction of upstream regulators following EV treatment, then trapped in the ECM. As with other solid cancers, aberrant WNT signaling in PDAC impacts tumor initiation and progression through many aspects such as cell survival, proliferation, differentiation, and drug resistance (58). A subpopulation of CAFs were found to express SFRP1/2 in a SOX-2 dependent manner to enhance colorectal cancer cell migration and invasion, in line with our findings (59). To our knowledge, our study is the first to show deposition of ECM with high SFRP1 by CAFs under the influence of TC-EVs, contributing to pro-tumoral actions of the ECM by promoting tumor cell migration and invasion. Functionally, SFRP1 had been long considered as an antagonist of WNT signaling pathway but is now recognized to have functions both as an agonist or an antagonist in a cell-type and concentration-dependent manner. Lower concentrations of SFRP1 in combination with a WNT pathway ligand, WNT3A, were found to stimulate instead of inhibit ß-catenin activity, mediated by frizzled-5 receptor. Since SFRP1 is also identified as an actor downstream of activated hedgehog signaling and a modulator of the TGFb1 pathway (60, 61), further mechanistic studies are required to delineate the specific role of SFRP1 in regulation of these compensatory pathways contributing to tumor cell aggressiveness.

Upon infiltration into tumor tissue, monocytes come into contact with the fibrotic ECM of the PDAC TME. It has been well established that the phenotype and function of various immune cells can be modulated by the characteristics of the ECM. Monocyte to macrophage differentiation was found to be impacted by the type of ECM substrate, such as collagen I or fibronectin in physiological and tumor contexts (62, 63) while M2-like polarization of macrophages was described in presence of hyaluronic acid or internalization of collagen I (64, 65). Since TC-EVs result in pro-tumoral CAF-ECMs, we investigated their influence on the differentiation of infiltrating monocytes and resulting macrophages. We observed that ECM produced by CAFs supplemented with recombinant SFRP1 (found enriched in TC-EVs treated CAFs derived ECM) demonstrated the differentiation of healthy monocytes to M2-like, immunosuppressive macrophages. Although Wnt signaling in macrophage differentiation and activity has been extensively studied in various contexts including cancer, the distinct macrophage polarization in response to canonical vs. non-canonical signaling have not yet been established, probably due to the variable repertoire of receptors on monocytes/macrophages and the context of Wnt signaling in presence of additional complementary signaling pathways.

Specifically, the role of SFRP1 in immune evasion through its impact on myeloid cells in PDAC is, we believe, unknown but the emergence of a pro-tumoral SFRP1^{+}-CAFs subtypes (59, 66), that we correlated to iCAFs using available public datasets, strengthen its suspected impact on immune evasion. Our study shows a novel role of SFRP1 on myeloid cell differentiation in presence of CAF-derived ECM, resulting in reduced T-cell activity. To further expand our findings, knockout of specific Wnt ligands or receptors on monocytes would highlight the mechanism by which Wnt ligands and their antagonists can mediate monocyte-to-macrophage differentiation and polarization.

This present proof-of-concept study highlights dual mechanisms of tumor cell-derived EVs on shaping the immunosuppressive landscape in PDAC, through direct and indirect influence on monocytes. Tumor cell-derived EVs drive monocytes-to-macrophages Alox15b^{+} polarization leading to T-cells inactivation (direct effect). In parallel, tumor cell-derived EVs induce CAFs reprogramming leading to SFRP1-enriched ECM secretion which consequently drive monocyte-to-macrophage polarization and T-cells inactivation (indirect effect). Expanding such findings to EVs derived from patient-derived tumor cells or patient-derived organoïds could highlight the potentially variable impacts of heterogeneous EVs populations on CAF-ECM production and monocyte-to-macrophage differentiation. Considering the critical impact of the immune-suppressive ecosystem in PDAC and its ability to hinder immune checkpoint inhibitors efficacy, unraveling new putative pathways and/or targets influencing such processes is of the greatest importance for PDAC patients. Hence, our findings suggested that limiting the impact of tumor cell derived EVs on monocyte and/or CAFs is of crucial interest in order to reduce PDAC immunosuppression.

Methods

Sex as a biological variable. Our study examined male and female human PDAC samples. Sex of PDAC patients was considered and did not appear as a biological variable.

Cell Culture. Cell Lines. Pancreatic epithelial ductal adenocarcinoma cell lines, PANC-1 (TC_1) and MiaPaCa-2 (TC_2), were obtained from American Type Culture Collection (Manassas, VA), CRL-1469 and CRL-1420 respectively, and cultured in Dulbecco's Modified Eagle's Medium (DMEM) Glutamax (Gibco) supplemented with 10% fetal bovine serum (FBS) (Biosera) and 1% antibiotic-antimycotic (Gibco). Non-tumor human pancreatic ductal epithelial cell line, hTERT-HPNE or HPDE, was obtained from ATCC, CRL-4023, and maintained in Keratinocyte Serum Free medium (K-SFM) supplemented with epidermal growth factor (EGF) and bovine pituitary extract (BPE) (Gibco). All cell lines were used for experiments until 20 rounds of passaging. Cell lines were detached using trypsin-EDTA 0.05% (Gibco) following a wash with 1x phosphate-buffered saline (PBS) and split at a 1:10 ratio.

Primary PDAC cancer-associated fibroblasts (CAFs) isolation and culture. Small pancreatic tissue blocks were obtained during pancreatic surgery from patients with resectable pancreatic adenocarcinoma at the Institute Paoli Calmettes (Marseille, France). The experimental procedure relating to the use of patient-derived pancreatic tumor pieces was performed after approval from the South Mediterranean Personal Protection Committee, under the reference 2011-A01439-32. Human primary CAFs were isolated as previously described (Leca et al., 2016). Briefly, the tumors were cut into small pieces of 1 mm^3 using a razor blade. The tissue pieces were dissociated using the Tumor Dissociation Kit (Miltenyi Biotec) according to the manufacturer's recommendations. Cells were then resuspended, passed through a cell strainer (100 μM), and finally plated. Human primary CAFs were used between passages 4 and 9. Primary CAF features were verified by flow cytometry with a positive α-SMA and FAP staining. Additional human primary CAFs used were a kind gift from Elisa Espinet Hernández, German Cancer Research Center (DKFZ, Heidelberg, Germany). All human primary CAFs were cultured in DMEM F-12 medium (Gibco) supplemented with 10% fetal bovine serum, 1% L-glutamine (Gibco), 1% antibiotic-antimycotic, and 0.5% sodium pyruvate (Gibco). Cells were detached and passaged using StemPro accutase cell dissociation reagent (Gibco).

Isolation of monocytes and T-cells. Healthy donor blood, in concentrated buffy coats, was obtained from the French Blood Establishment (Marseille, France). The blood from a total of 68 healthy donors were used throughout the different experiments in the whole study. Peripheral blood mononuclear cells (PBMC) were isolated using the Ficoll-Paque density gradient method. Briefly, buffy coats were mixed with RPMI 1640 medium (Gibco) supplemented with 10% FBS and 1% antibiotic-antimycotic and centrifuged at 400 x g for 40 minutes (with 0 acceleration and deceleration) with Ficoll-Paque (Cytvia) to obtain a ring of PBMCs. This ring was isolated, incubated for 10 minutes in 1x red blood cell lysis buffer (eBioscience) and washed in 1X PBS 4 times before cell counting. CD14+ monocytes were isolated from PBMCs using magnetic labeling and sorting with human CD14 microbeads (Miltenyi Biotec) by positive selection following the manufacturer's protocol and the autoMacs pro separator (Miltenyi Biotec). Pan T-cells were isolated from PBMCs using magnetic labeling and sorting by negative selection with the Pan T-cell isolation kit (Miltenyi Biotec) following the manufacturer's protocol. Purity of isolated monocytes and pan T-cells was verified using flow cytometry staining and analysis of CD14 and CD3 marker expression respectively. Pan T-cells were activated and expanded for 48h using T-cell Transact, CD3/CD28 stimulation reagent (Miltenyi Biotec) and 40ng/mL of IL-2 (Miltenyi Biotec).

All cultured cells were tested for mycoplasma contamination using MycoAlert Mycoplasma Detection Kit (Lonza). For treatment with EVs, recipient cells were cultured in EVs-free media, where appropriate medium was supplemented with FBS previously ultra-centrifuged at 100,000 x g for 18 hours to remove FBS-sourced EVs.

EVs isolation and characterization. Extracellular vesicles were isolated from supernatants of PANC-1 (TC_1), MiaPaCa-2 (TC_2) and HPDE cell lines and primary PDAC organoid cultures as well as their respective cell-culture medium as controls. Cancer cell lines, PANC-1 and

MiaPaCa-2 cells were plated and once at 70-80% confluency, their medium was refreshed 24h before collection of supernatants to DMEM without FBS supplemented with 1% antibiotic-antimycotic. HPDE cells medium was changed to their classic medium, as noted above, at 70-80% confluency 24h before collection. Supernatants were collected and centrifuged at 500 x g for 5 minutes to remove dead cells and debris. The supernatants were then centrifuged at 100, 000 x g for 90 minutes at 4°C using the OptimaMax XP Ultracentrifuge (Beckman Coulter, USA). Pellets were collected in 500µL 1x PBS and loaded onto a qEVoriginal 70nm column (Izon) to separate vesicles by size-exclusion chromatography (SEC). The column was washed with 15 mL of 1x PBS and 500µL fractions, fractions 7-10, were collected and pooled. Pooled fractions were washed by centrifugation at 100 000 x g for 90 minutes. Resulting pellets were resuspended in 50-100µL, depending on the experiment, before treatment. Average cell counts per 10mL of cell culture supernatant per 1 T75 flask for EV collection were: $2.19E10^6$ for PANC-1, $5.36E10^6$ for MiaPaCa-2, and $3.89E10^6$ for HPDE. These cell counts allowed for isolation of average $1.07E10^9$ EV particles for PANC-1, $5.09E10^8$ for MiaPaCa-2 and $5.84E10^8$ for HPDE. For monocyte EV-treatments, 500.000 monocytes were treated with an average of $5.35E10^8$ particles of EVs isolated from 5mL of cell culture supernatants from PANC-1, 10ml from MiaPaCa-2 and 9ml from HPDE (for the ratio 2:1). For CAF-EV treatments, 100.000 CAFs were treated with an average of $1.07E10^8$ particles of EVs isolated from 1mL of cell culture supernatants from PANC-1, 2ml from MiaPaCa-2 and 1.8ml from HPDE (for the ratio 2:1). Various ratio 1:1, 2:1, 5:1 and 10:1 were investigated. This ratio was associated with a define number of EVs for PANC-1 and we normalized the experiments with other producing cells by comparing the same number of EVs. This lead to a variation in volume used between cell lines but no variation in EVs added during the treatments.

Isolated extracellular vesicles were characterized for their size and concentration using nanoparticle tracking analysis on the Nanosight NS300 instrument (Malvern Panalytical, UK). Samples were diluted 5-fold in a final volume of 500µL. Ideal measurement settings and concentrations were found by pre-testing the ideal particle per frame value (20–60 particles/frame). Camera level was increased and focus adjusted until all particles were visible. For all measurements, three 1-minute videos were captured at 25°C in order to calculate mean values of particle concentration and size. Isolated extracellular vesicles were further characterized for each cell line using Western blot for detection of classic EVs markers: Alix, Tsg-101, syntenin, CD63, CD81, and CD9 (see Table 1 for primary antibody details).

We have submitted all relevant data from our experiments and all information of PANC-1, MiaPaCa-2 and HPDE EVs to the EV-TRACK knowledgebase (EV-TRACK ID : EV260025).

Treatment of Monocytes with EVs, and Cocultures. Following CD14+ monocyte isolation from PBMCs, monocytes were plated at a density of 500,000 cells per well in 24-well plates in complete RPMI medium containing FBS depleted of EVs. Monocytes were treated with PANC-1, MiaPaCa-2 or HPDE EVs for two consecutive days, plated in EV-depleted supernatant or culture medium (1:2 with RPMI), or treated with 40ng/mL of MCSF once (Miltenyi Biotec). Two days following the last EVs treatment, differentiated macrophages of all conditions were detached and counted. For recombinant protein treatments, recombinant SFRP1 or Wnt5a was added to wells of monocytes at 1µg/mL and 500 ng/mL respectively. For all other assays, macrophages were analyzed by live-cell imaging for viability and phagocytic activity or detached and marked for immunophenotyping by flow cytometry five days following the last EVs treatment.

For T-cell assays, detached macrophages were placed into 1:1 cocultures with same-donor isolated pan T-cells for 3 days. For the T-cell proliferation assay, pan T-cells were marked before coculture with Cell-trace Violet as described below. Following coculture, pan T-cells were isolated by recovering cells in suspension, washing wells twice with PBS and recovering cells from washes. Unstimulated pan T-cells without TransAct, and activated T-cells with TransAct in simple culture were used as controls. Following one wash in complete RPMI medium, pan T-cells were either analyzed by flow cytometry for proliferation assays or counted

for subsequent coculture with tumor cells, PANC-1 and MiaPaCa-2, in complete RPMI at a ratio of 1:5 (tumor cell: T-cell) for a duration of 3 days.

Extended methods. Additional details on reagents, assays and bioinformatics analysis are described in the Supplemental Methods.

Statistical analyses. Statistics were performed on GraphPad Prism 8 for all statistical tests unless, otherwise stated below, using two-tailed unpaired non-parametric student's t-tests with Welch's correction, Mixed-effects analysis with uncorrected Fisher's LSD for multiple comparisons test or one-way ANOVA (nonparametric) with Kruskal-Wallis test and Dunn's multiple comparisons test. For experiments comparing more than 2 conditions, without missing values, we performed one-way ANOVA test and for experiments comparing more than 2 conditions, with missing values for completely random reason, we performed Mixed-effects analysis. For those experiments, in figures and legends, stars refer to the adjusted P value from Dunn's multiple comparisons test or uncorrected Fisher's LSD multiple comparisons test while the one-way ANOVA (Kruskal-Wallis test) and Mixed-effects analysis P value is added directly into the figure. *P-values* < 0.05 were considered statistically significant. Statistical analysis of mass spectrometry data was done with Perseus program (version 1.6.15.0) from the MaxQuant environment. Quantifiable proteins were defined as those detected in above 70% of samples in one condition or more. Protein LFQ normalized intensities were base 2-logarithmized to obtain a normal distribution. Missing values were replaced using data imputation by randomly selecting from a normal distribution centered on the lower edge of the intensity values that simulates signals of low abundant proteins using default parameters (a downshift of 1.8 standard deviation and a width of 0.3 of the original distribution). To determine whether a given detected protein was specifically differential, a two-sample t-test was done using permutation-based FDR-controlled at 0.05 and employing 250 permutations. The p-value was adjusted using a scaling factor s0 with a value of 1. Analysis was done on biological triplicates, each injected three times on mass spectrometers.

AUTHOR CONTRIBUTIONS

Conception and design: ZH, RT

Development of methodology: ZH, CM, CR, DB, SST, PF, TB, EL, SA, LC, MR, DI

Acquisition of data (provided animals, acquired and managed patients, provided facilities, etc.): ZH, CM, CR, DB, SST, PF, FB, SA, MR, DI

Analysis and interpretation of data (e.g., statistical analysis, biostatistics, computational analysis): ZH, CM, CR, DB, MR, LC, PF, FB, RT

Administrative, technical or material support (i.e., reporting or organizing data, constructing databases): ZH, MR, SV, FB, RT, SA

Study supervision: RT

Writing original draft: ZH, MR, RT

Writing revised draft: ZH, CM, MR, RT

ACKNOWLEDGEMENTS

We would like to thank Rania Ghossoub and Alix Nicolas for technical support. We also thank the CRCM shared resources: Victor Pierini and Regis Vitestelle for the PSEA animal facility, Michel Baccini and Gagik Hovhannisyan for informatical support, Thi-tien NGuyen for the Cell Culture Platform, Bruno Olivier and Tahagan Titus for technical assistance. The electron microscopy experiments were performed on the PICsL-FBI core facility (Nicolas Brouilly, Fabrice Richard, IBDM, AMU-Marseille), member of the France-BioImaging national research infrastructure (ANR-24-INBS-0005). The authors acknowledge Anais Berger from the CEEVEC platform, and the Cancéropôle Provence-Alpes-Côte d'Azur.

FUNDING SUPPORT

- Ministère Français de la recherche, PhD fellowship (to ZH)
- Fondation de France, grant « fundamental and translationnal research on cancer : study of treatment resistance », 00087538 (to TB)
- Fondation de France, grant « fundamental and translationnal research on cancer : study of treatment resistance », 00130850 and 00156332 (to CR)
- The French National Institute of Cancer, INCA, *PLBio13-134* and Pancreas *2017* (to SST and RT)
- The fondation ARC pour la Recherche sur le Cancer, ARC PGA 2020 (to SV)
- The fondation ARC pour la Recherche sur le Cancer, ARC Pancreas, ARCPANCREAS2024, 040008193 (to RT)
- The fondation ARC pour la Recherche sur le Cancer, ARC PJA, 20191209372 (to RT)
- The National League Against Cancer, EL-2025.LNCC (to SV)
- The National League Against Cancer, PhD fellowship, TAJG28258 (to DB)
- The National League Against Cancer, PhD Fourth year, TDQA22676 (to ZH)
- The Association Française de Recherche sur le cancer du pancréas, AFRCP (to CM)
- CAPES grant, 88887.466422/2019-00 and 88881.711952/2022-01 (to MR)
- CNPq grant, 442179/2023-5, 203087/2019-4, 312426/2021-7 (to MR) and 200052/2024-1 (to CM)

DATA MATERIALS AVAILABILITY

All data are available in the main text, supplement, and Supporting Data Values. The mass spectrometry proteomics data have been deposited to the ProteomeXchange Consortium via the PRIDE partner repository with the dataset identifier PXD039279 and PXD039439 (67).

References

1. Sung H, et al. Global Cancer Statistics 2020: GLOBOCAN Estimates of Incidence and Mortality Worldwide for 36 Cancers in 185 Countries. *CA Cancer J Clin*. 2021;71 (3):209–249.
2. Shinde RS, et al. Cutting-edge strategies for borderline resectable pancreatic cancer. *Ann Gastroenterol Surg*. 2019;3 (4):368–372.
3. Principe DR, et al. Trials and tribulations of pancreatic cancer immunotherapy. *Cancer Lett*. 2021;504:1–14.
4. Geng X, et al. Cancer-Associated Fibroblast (CAF) Heterogeneity and Targeting Therapy of CAFs in Pancreatic Cancer. *Front Cell Dev Biol*. 2021;9 (July):1–14.
5. Pereira BA, et al. CAF Subpopulations: A New Reservoir of Stromal Targets in Pancreatic Cancer. *Trends Cancer*. 2019;5 (11):724–741.
6. Muller M, et al. The Immune Landscape of Human Pancreatic Ductal Carcinoma: Key Players, Clinical Implications, and Challenges. *Cancers (Basel)*. 2022;14 (4). https://doi.org/10.3390/cancers14040995.
7. Ullman NA, et al. Immunologic Strategies in Pancreatic Cancer: Making Cold Tumors Hot. *J Clin Oncol*. 2022;40 (24):2789–2805.
8. Zhao W, et al. Galectin-3 Mediates Tumor Cell-Stroma Interactions by Activating Pancreatic Stellate Cells to Produce Cytokines via Integrin Signaling. *Gastroenterology*. 2018;154 (5):1524-1537.e6.
9. Xiao Q, et al. Cancer-Associated Fibroblasts in Pancreatic Cancer Are Reprogrammed by Tumor-Induced Alterations in Genomic DNA Methylation. *Cancer Res*. 2016;76 (18):5395–5404.
10. Nan P, et al. Tumor-stroma TGF-β1-THBS2 feedback circuit drives pancreatic ductal adenocarcinoma progression via integrin α (v)β (3)/CD36-mediated activation of the MAPK pathway. *Cancer Lett*. 2022;528:59–75.
11. Rossi Sebastiano M, et al. ACSL3-PAI-1 signaling axis mediates tumor-stroma cross-talk promoting pancreatic cancer progression. *Sci Adv*. 2020;6 (44). https://doi.org/10.1126/sciadv.abb9200.
12. Liu X, et al. The Crosstalk Between Malignant Cells and Tumor-Promoting Immune Cells Relevant to Immunotherapy in Pancreatic Ductal Adenocarcinoma. *Front Cell Dev Biol*. 2021;9:821232.
13. Zaborowski MP, et al. Extracellular Vesicles: Composition, Biological Relevance, and Methods of Study. *Bioscience*. 2015;65 (8):783–797.
14. Costa-Silva B, et al. Pancreatic cancer exosomes initiate pre-metastatic niche formation in the liver. *Nat Cell Biol*. 2015;17 (6):816–826.
15. Chen K, et al. Hypoxic pancreatic cancer derived exosomal miR-30b-5p promotes tumor angiogenesis by inhibiting GJA1 expression. *Int J Biol Sci*. 2022;18 (3):1220–1237.
16. Zhao J, et al. Tumor-Derived Extracellular Vesicles Inhibit Natural Killer Cell Function in Pancreatic Cancer. *Cancers (Basel)*. 2019;11 (6). https://doi.org/10.3390/cancers11060874.
17. Fan J, et al. Chemoresistance Transmission via Exosome-Mediated EphA2 Transfer in Pancreatic Cancer. *Theranostics*. 2018;8 (21):5986–5994.
18. Patel GK, et al. Exosomes confer chemoresistance to pancreatic cancer cells by promoting ROS detoxification and miR-155-mediated suppression of key gemcitabine-metabolising enzyme, DCK. *Br J Cancer*. 2017;116 (5):609–619.
19. Vayrynen SA, et al. Composition, Spatial Characteristics, and Prognostic Significance of Myeloid Cell Infiltration in Pancreatic Cancer. *Clinical Cancer Research*. 2021;27 (4):1069–1081.
20. Dong L, et al. SFRP1 mediates cancer-associated fibroblasts to suppress cancer cell proliferation and migration in head and neck squamous cell carcinoma. *BMC Cancer*. 2024;24 (1):1165.
21. Jenkins BH, et al. Single cell and spatial analysis of immune-hot and immune-cold tumours identifies fibroblast subtypes associated with distinct immunological niches and positive immunotherapy response. *Mol Cancer*. 2025;24 (1):3.
22. Birnbaum DJ, et al. Validation and comparison of the molecular classifications of pancreatic carcinomas. [preprint]. *Mol Cancer*. 2017;16 (1):168.
23. Picard FSR, et al. IL-17A-producing CD8 (+) T cells promote PDAC via induction of inflammatory cancer-associated fibroblasts. *Gut*. 2023;72 (8):1510–1522.
24. Bengtsson A, Andersson R, Ansari D. The actual 5-year survivors of pancreatic ductal adenocarcinoma based on real-world data. *Sci Rep*. 2020;10 (1):16425.
25. Shao S, Miao H, Ma W. Unraveling the enigma of tumor-associated macrophages: challenges, innovations, and the path to therapeutic breakthroughs. *Front Immunol*. 2023;14:1295684.
26. Yu B, Shao S, Ma W. Frontiers in pancreatic cancer on biomarkers, microenvironment, and immunotherapy. *Cancer Lett*. 2025;610:217350.
27. Thomas D, Radhakrishnan P. Tumor-stromal crosstalk in pancreatic cancer and tissue fibrosis. *Mol Cancer*. 2019;18 (1):14.
28. Murphy KJ, et al. Dynamic Stromal Alterations Influence Tumor-Stroma Crosstalk to Promote Pancreatic Cancer and Treatment Resistance. *Cancers (Basel)*. 2021;13 (14). https://doi.org/10.3390/cancers13143481.
29. Marzan AL, Stewart SE. Elucidating the Role of Extracellular Vesicles in Pancreatic Cancer. *Cancers (Basel)*. 2021;13 (22). https://doi.org/10.3390/cancers13225669.

30. Chen S, et al. Peripheral blood monocytes predict clinical prognosis and support tumor invasiveness through NF-κB-dependent upregulation of Snail in pancreatic cancer. *Transl Cancer Res*. 2021;10 (11):4773–4785.
31. Kemp SB, et al. Pancreatic cancer is marked by complement-high blood monocytes and tumor-associated macrophages. *Life Sci Alliance*. 2021;4 (6). https://doi.org/10.26508/lsa.202000935.
32. Li X, et al. CCL2-mediated monocytes regulate immune checkpoint blockade resistance in pancreatic cancer. *Int Immunopharmacol*. 2022;106:108598.
33. Huang C, et al. Interleukin 35 Expression Correlates With Microvessel Density in Pancreatic Ductal Adenocarcinoma, Recruits Monocytes, and Promotes Growth and Angiogenesis of Xenograft Tumors in Mice. *Gastroenterology*. 2018;154 (3):675–688.
34. Zhu Y, et al. Tissue-Resident Macrophages in Pancreatic Ductal Adenocarcinoma Originate from Embryonic Hematopoiesis and Promote Tumor Progression. *Immunity*. 2017;47 (2):323-338.e6.
35. Baj-Krzyworzeka M, et al. The role of CD44H molecule in the interactions between human monocytes and pancreatic adenocarcinoma-derived microvesicles. *Folia Histochem Cytobiol*. 2019;57 (1):28–34.
36. Patel AA, et al. The fate and lifespan of human monocyte subsets in steady state and systemic inflammation. *J Exp Med*. 2017;214 (7):1913–1923.
37. Song X, et al. Cancer Cell-derived Exosomes Induce Mitogen-activated Protein Kinase-dependent Monocyte Survival by Transport of Functional Receptor Tyrosine Kinases. *J Biol Chem*. 2016;291 (16):8453–8464.
38. Hu H, et al. The combination of PKM2 overexpression and M2 macrophages infiltration confers a poor prognosis for PDAC patients. *J Cancer*. 2020;11 (8):2022–2031.
39. Ji H, et al. Integrated genomic, transcriptomic, and epigenetic analyses identify a leukotriene synthesis-related M2 macrophage gene signature that predicts prognosis and treatment vulnerability in gliomas. *Front Immunol*. 2022;13:970702.
40. Daurkin I, et al. Tumor-Associated Macrophages Mediate Immunosuppression in the Renal Cancer Microenvironment by Activating the 15-Lipoxygenase-2 Pathway. *Cancer Res*. 2011;71 (20):6400–6409.
41. Liu B, et al. Tumor-associated macrophage-derived CCL20 enhances the growth and metastasis of pancreatic cancer. *Acta Biochim Biophys Sin (Shanghai)*. 2016;48 (12):1067–1074.
42. Ye H, et al. Tumor-associated macrophages promote progression and the Warburg effect via CCL18/NF-kB/VCAM-1 pathway in pancreatic ductal adenocarcinoma. *Cell Death Dis*. 2018;9 (5):453.
43. Sun X, et al. Inflammatory cell-derived CXCL3 promotes pancreatic cancer metastasis through a novel myofibroblast-hijacked cancer escape mechanism. *Gut*. 2022;71 (1):129–147.
44. Pausch TM, et al. Metastasis-associated fibroblasts promote angiogenesis in metastasized pancreatic cancer via the CXCL8 and the CCL2 axes. *Sci Rep*. 2020;10 (1):5420.
45. Sharma V, et al. CCR4 (+) monocytic myeloid-derived suppressor cells are associated with the increased epithelial-mesenchymal transition in pancreatic adenocarcinoma patients. *Immunobiology*. 2022;227 (3):152210.
46. Kalbasi A, et al. Tumor-Derived CCL2 Mediates Resistance to Radiotherapy in Pancreatic Ductal Adenocarcinoma. *Clin Cancer Res*. 2017;23 (1):137–148.
47. Gu H, et al. CCL2 produced by pancreatic ductal adenocarcinoma is essential for the accumulation and activation of monocytic myeloid-derived suppressor cells. *Immun Inflamm Dis*. 2021;9 (4):1686–1695.
48. Feng L, et al. Serum level of ccl2 predicts outcome of patients with pancreatic cancer. *Acta Gastroenterol Belg*. 2020;83 (2):295–299.
49. Malik S, et al. CXCL12 in Pancreatic Cancer: Its Function and Potential as a Therapeutic Drug Target. *Cancers (Basel)*. 2021;14 (1). https://doi.org/10.3390/cancers14010086.
50. Balachandran VP, Beatty GL, Dougan SK. Broadening the Impact of Immunotherapy to Pancreatic Cancer: Challenges and Opportunities. *Gastroenterology*. 2019;156 (7):2056–2072.
51. Leppänen J, et al. Tenascin C, Fibronectin, and Tumor-Stroma Ratio in Pancreatic Ductal Adenocarcinoma. *Pancreas*. 2019;48 (1):43–48.
52. Hu D, et al. Stromal fibronectin expression in patients with resected pancreatic ductal adenocarcinoma. *World J Surg Oncol*. 2019;17 (1):29.
53. Wang K, et al. Breast cancer cells alter the dynamics of stromal fibronectin-collagen interactions. *Matrix Biol*. 2017;60–61:86–95.
54. Erdogan B, et al. Cancer-associated fibroblasts promote directional cancer cell migration by aligning fibronectin. *Journal of Cell Biology*. 2017;216 (11):3799–3816.
55. Miyazaki K, et al. Collective cancer cell invasion in contact with fibroblasts through integrin-α5β1/fibronectin interaction in collagen matrix. *Cancer Sci*. 2020;111 (12):4381–4392.
56. Öhlund D, et al. Type IV collagen stimulates pancreatic cancer cell proliferation, migration, and inhibits apoptosis through an autocrine loop. *BMC Cancer*. 2013;13:154.
57. Yousif NG. Fibronectin promotes migration and invasion of ovarian cancer cells through up-regulation of FAK-PI3K/Akt pathway. *Cell Biol Int*. 2014;38 (1):85–91.
58. Aguilera KY, Dawson DW. WNT Ligand Dependencies in Pancreatic Cancer. *Front Cell Dev Biol*. 2021;9:671022.
59. Kasashima H, et al. Stromal SOX2 Upregulation Promotes Tumorigenesis through the Generation of a SFRP1/2-Expressing Cancer-Associated Fibroblast Population. *Dev Cell*. 2021;56 (1):95-110.e10.
60. Katoh Y, Katoh M. WNT antagonist, SFRP1, is Hedgehog signaling target. *Int J Mol Med*. 2006;17 (1):171–175.

61. Peng J-X, Liang S-Y, Li L. sFRP1 exerts effects on gastric cancer cells through GSK3β/Rac1-mediated restraint of TGFβ/Smad3 signaling. *Oncol Rep*. 2019;41 (1):224–234.
62. Jacob SS, Shastry P, Sudhakaran PR. Monocyte-macrophage differentiation in vitro: modulation by extracellular matrix protein substratum. *Mol Cell Biochem*. 2002;233 (1–2):9–17.
63. Kamoshida G, et al. Monocyte differentiation induced by co-culture with tumor cells involves RGD-dependent cell adhesion to extracellular matrix. *Cancer Lett*. 2012;315 (2):145–152.
64. Kim H, et al. Hyaluronic acid-based extracellular matrix triggers spontaneous M2-like polarity of monocyte/macrophage. *Biomater Sci*. 2019;7 (6):2264–2271.
65. LaRue MM, et al. Metabolic reprogramming of tumor-associated macrophages by collagen turnover promotes fibrosis in pancreatic cancer. *Proc Natl Acad Sci U S A*. 2022;119 (16):e2119168119.
66. Li E, Cheung HCZ, Ma S. CTHRC1 (+) fibroblasts and SPP1 (+) macrophages synergistically contribute to pro-tumorigenic tumor microenvironment in pancreatic ductal adenocarcinoma. *Sci Rep*. 2024;14 (1):17412.
67. Perez-Riverol Y, et al. The PRIDE database resources in 2022: a hub for mass spectrometry-based proteomics evidences. *Nucleic Acids Res*. 2021;50 (D1):D543–D552.

Figure 1.
Hussain et al.

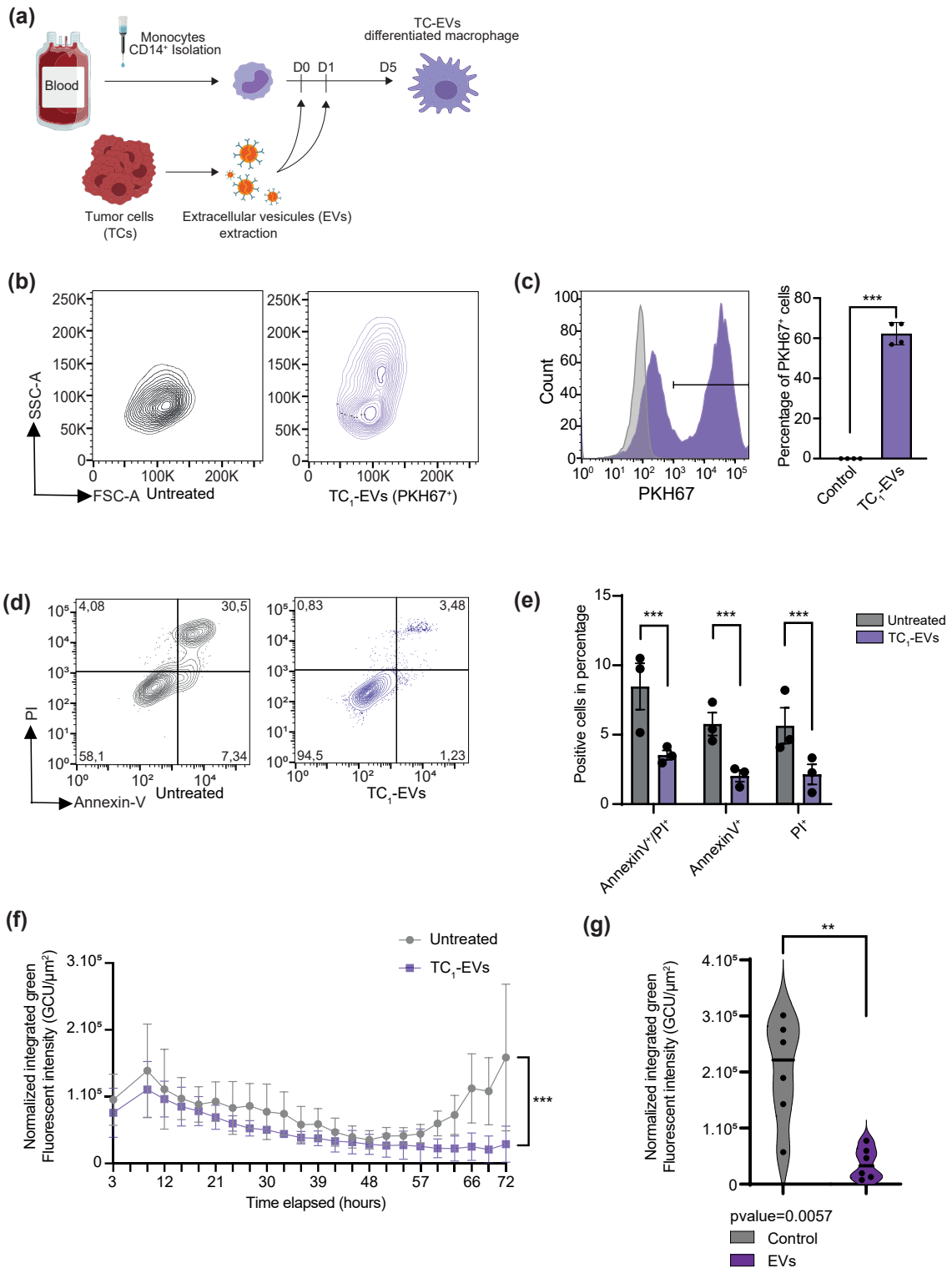

Figure 1. PDAC tumor cell (TC)-EVs are efficiently internalized by monocytes and confer increased viability. (A) Schematic depiction of experimental protocol: healthy blood donor buffy coats were used to extract peripheral blood mononuclear cells (PBMCs) and monocytes were isolated using CD14+ magnetic beads. TC-EVs were extracted from TCs (TC_1) conditioned medium and monocytes were treated for two consecutive days and incubated for a total of 5 days before analysis. **(B)** Representative flow cytometry graphs of forward- and side-scatter of untreated and TC_1-EVs-treated monocytes 24h following treatment (N=4). **(C)** Representative histogram of monocyte internalization of PKH67-GFP labelled TC_1-EVs by untreated and treated monocytes (left), 24h following treatments. Percentage of total cell population with internalized PKH67-GFP labelled EVs between untreated and TC_1-EVs treated monocytes (right), 24h following treatments (N=4). **(D)** Representative flow cytometry plots of annexin-V and propidium iodide (PI) staining of TC_1-EVs treated monocytes following 96h of treatment (N=3). **(E)** Percentage of total monocytes expressing annexin-V, PI, or double-positive for annexin-V/PI in untreated and TC_1-EVs treated monocytes (N=3). **(F)** Normalized fluorescent green integrated intensity (GCU/μm^2) of monocytes marked with dead-cell marking agent, Cytotox Green (Incucyte), in untreated and TC_1-EVs treated monocytes over a 72h period analyzed by live-cell imaging (N=3). **(G)** Normalized fluorescent green integrated intensity (GCU/μm^2) of Cytotox Green in untreated or TC_1-EVs treated monocytes at the 72h timepoint (N=3). Statistical analyses were performed using paired student's t-tests. Significant differences in expression with p-values <0.0001 ****, <0.001 ***, <0.01 **, and <0.05 * are indicated.

Figure 2.
Hussain et al.

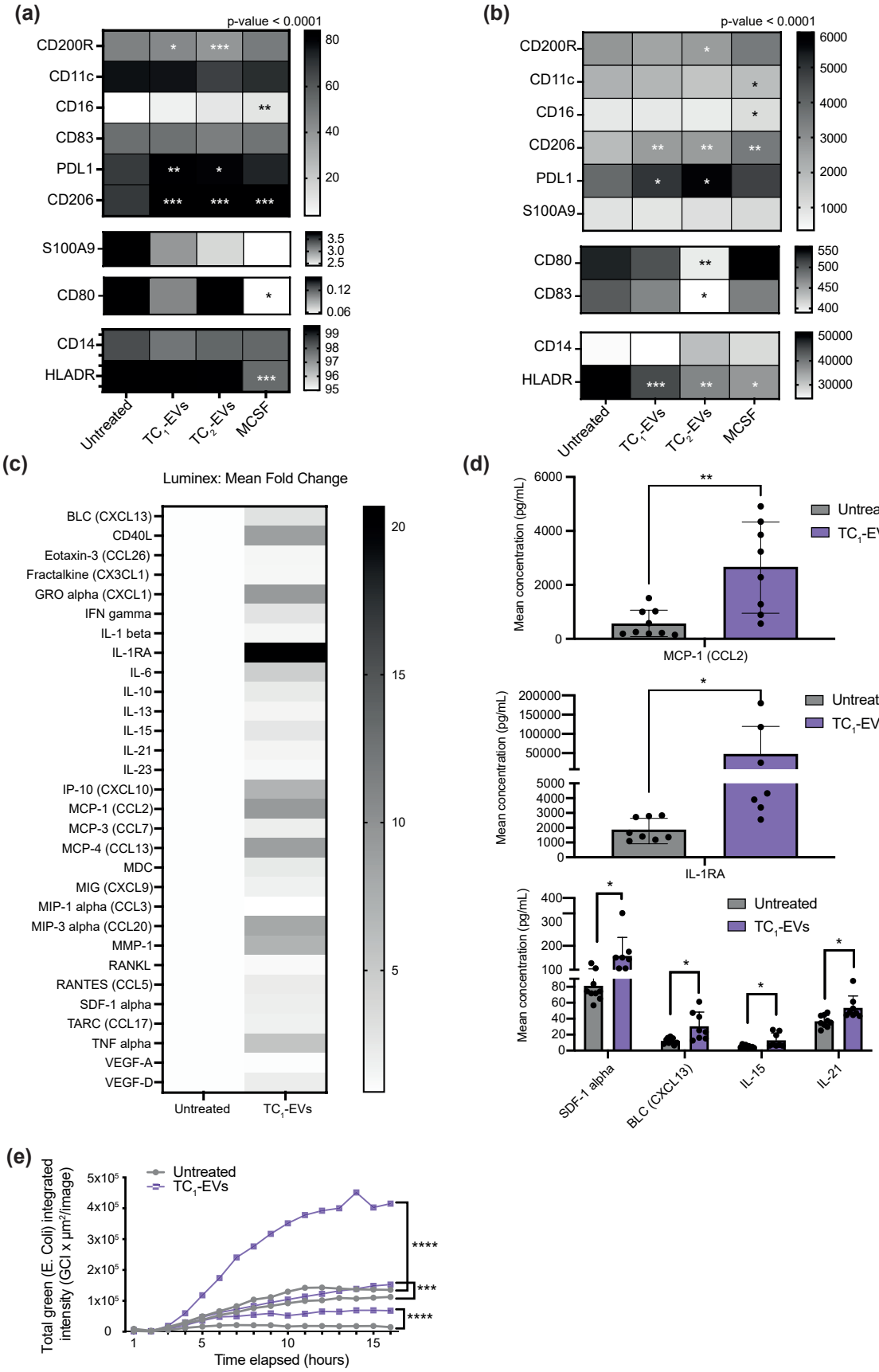

Figure 2. PDAC TC-EVs differentiate healthy monocytes to M2-like immunosuppressive macrophages. (A) Heat maps depicting multiparametric flow cytometry analysis of percentage of total cell populations expressing markers for monocyte/macrophages, M1-macrophages, M2-macrophages, and MDSCs between untreated, TC_1-, TC_2-EVs differentiated macrophages, and M-CSF (40ng/mL) differentiated macrophages following the experimental protocol in Fig 1A (N=9 to 22). **(B)** Heat map of median fluorescence intensities (MFI) of the markers shown in Fig 2A (N=9 to 22). **(C)** Multiplex-ELISA (Luminex) analysis of 30 cytokines and chemokines secreted by untreated and TC_1-EVs differentiated macrophages (N=3). **(D)** Significantly upregulated cytokines and chemokines secreted by untreated and TC_1-EVs differentiated macrophages (N=3). **(E)** Phagocytosis of fluorescent green E. coli bioparticles by untreated and TC_1-EVs differentiated macrophages from three healthy donor-derived monocytes analyzed by live-cell imaging over 16 hours (N=3). Statistical analyses were performed using Mixed-effects analysis with uncorrected Fisher's LSD for multiple comparisons test (A and B) and paired student's t-tests (D and E). Significant differences with p-values <0.0001 ****, <0.001 ***, <0.01 **, and <0.05 * are indicated.

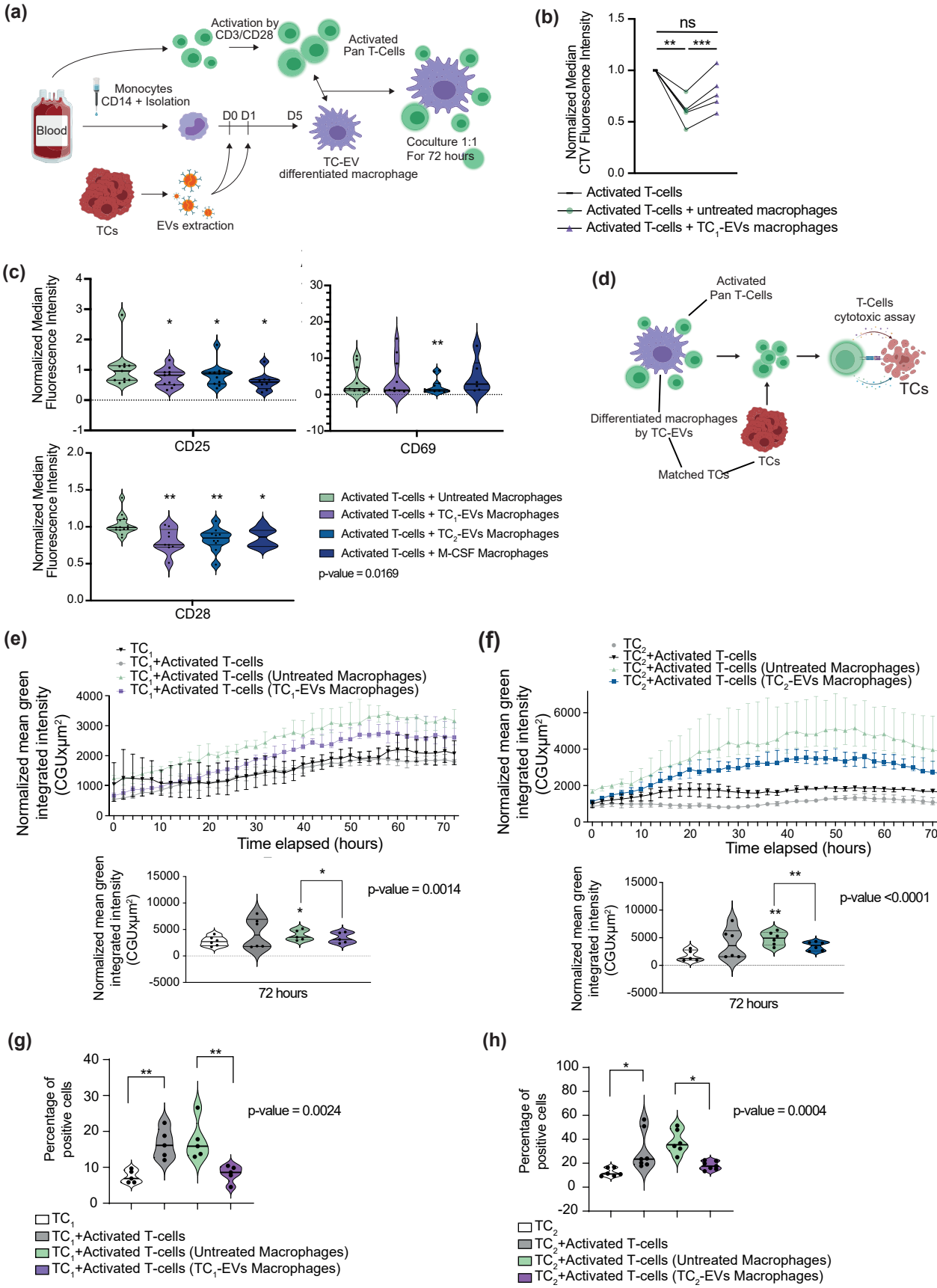
(a)
Activation by CD3/CD28
Activated Pan T-Cells
Monocytes CD14 + Isolation
Blood
D0 D1
D5
Coculture 1:1 For 72 hours
TC-EV differentiated macrophage
TCs
EVs extraction
(b)
Normalized Median CTV Fluorescence Intensity
ns
**
***
Activated T-cells
Activated T-cells + untreated macrophages
Activated T-cells + TC1-EVs macrophages
(c)
Normalized Median Fluorescence Intensity
CD25
CD69
CD28
Activated T-cells + Untreated Macrophages
Activated T-cells + TC1-EVs Macrophages
Activated T-cells + TC2-EVs Macrophages
Activated T-cells + M-CSF Macrophages
p-value = 0.0169
(d)
Activated Pan T-Cells
T-Cells cytotoxic assay
TCs
Differentiated macrophages by TC-EVs
TCs
Matched TCs
(e)
TC1
TC1+Activated T-cells
TC1+Activated T-cells (Untreated Macrophages)
TC1+Activated T-cells (TC1-EVs Macrophages)
Normalized mean green integrated intensity (CGUxμm2)
Time elapsed (hours)
72 hours
p-value = 0.0014
(f)
TC2
TC2+Activated T-cells
TC2+Activated T-cells (Untreated Macrophages)
TC2+Activated T-cells (TC2-EVs Macrophages)
Normalized mean green integrated intensity (CGUxμm2)
Time elapsed (hours)
72 hours
p-value <0.0001
(g)
Percentage of positive cells
p-value = 0.0024
TC1
TC1+Activated T-cells
TC1+Activated T-cells (Untreated Macrophages)
TC1+Activated T-cells (TC1-EVs Macrophages)
(h)
Percentage of positive cells
p-value = 0.0004
TC2
TC2+Activated T-cells
TC2+Activated T-cells (Untreated Macrophages)
TC2+Activated T-cells (TC2-EVs Macrophages)

Figure 3. PDAC TC-EVs differentiated macrophages suppress T-cell proliferation, activation, and cytotoxic activity against tumor cells. (A) Schematic depiction of experimental protocol: Healthy blood donor-derived monocytes were isolated and treated with TC-EVs as described in Fig 1A. Same donor pan T-cells were isolated using negative magnetic selection and activated using CD3/CD28 (TransAct) for 48 hours. Untreated or TC-EVs differentiated macrophages were placed in coculture at a 1:1 ratio with activated T-cells for 72 hours. **(B)** Proliferation assay of T-cells in coculture with macrophages: fold change of MFI of Cell-Trace Violet expression in T-cells in coculture with untreated or TC_1-EVs differentiated macrophages, normalized to MFI of monoculture T-cells (N=5). **(C)** Normalized MFI of T-cell activation markers (CD25 and CD69) and co-stimulatory marker (CD28) in T-cells cocultured with untreated, TC_1-EVs-treated, TC_2-EVs treated, and MCSF-treated macrophages, analyzed by flow cytometry (N=4). **(D)** Schematic depiction of tumor cell killing/T-cell cytotoxicity assay where T cells from macrophage cocultures were isolated and placed in coculture with TCs at a 5:1 ratio. **(E)** Caspase 3/7 activity of TC_1 (N=5) and **(F)** TC_2 (N=6) following coculture with monoculture activated T-cells, cocultured T-cells with untreated macrophages, and with TC_1- or TC_2-EVs differentiated macrophages analyzed by live-cell imaging over 72 hours (N=5) (top). Graphs of caspase 3/7 activity of both TCs in above conditions at the 72 hours timepoint (bottom). **(G and H)** Total percentage of TC_1 (**G**, N=5) and TC_2 (**H**, N=6 or 7) positive cells for Annexin V, for propidium iodide (PI) and double positive for Annexin V/PI following cocultures with above-described T-cell conditions analyzed by flow cytometry. Statistical analyses were performed using paired student's t-tests (B), Mixed-effects analysis with uncorrected Fisher's LSD for multiple comparisons test (C), one-way non-parametric ANOVA Kruskal-Wallis test and Dunn's multiple comparisons tests (E-H). Significant differences with p-values <0.0001 ****, <0.001 ***, <0.01 **, and <0.05 * are indicated.

Figure 4.
Hussain et al.

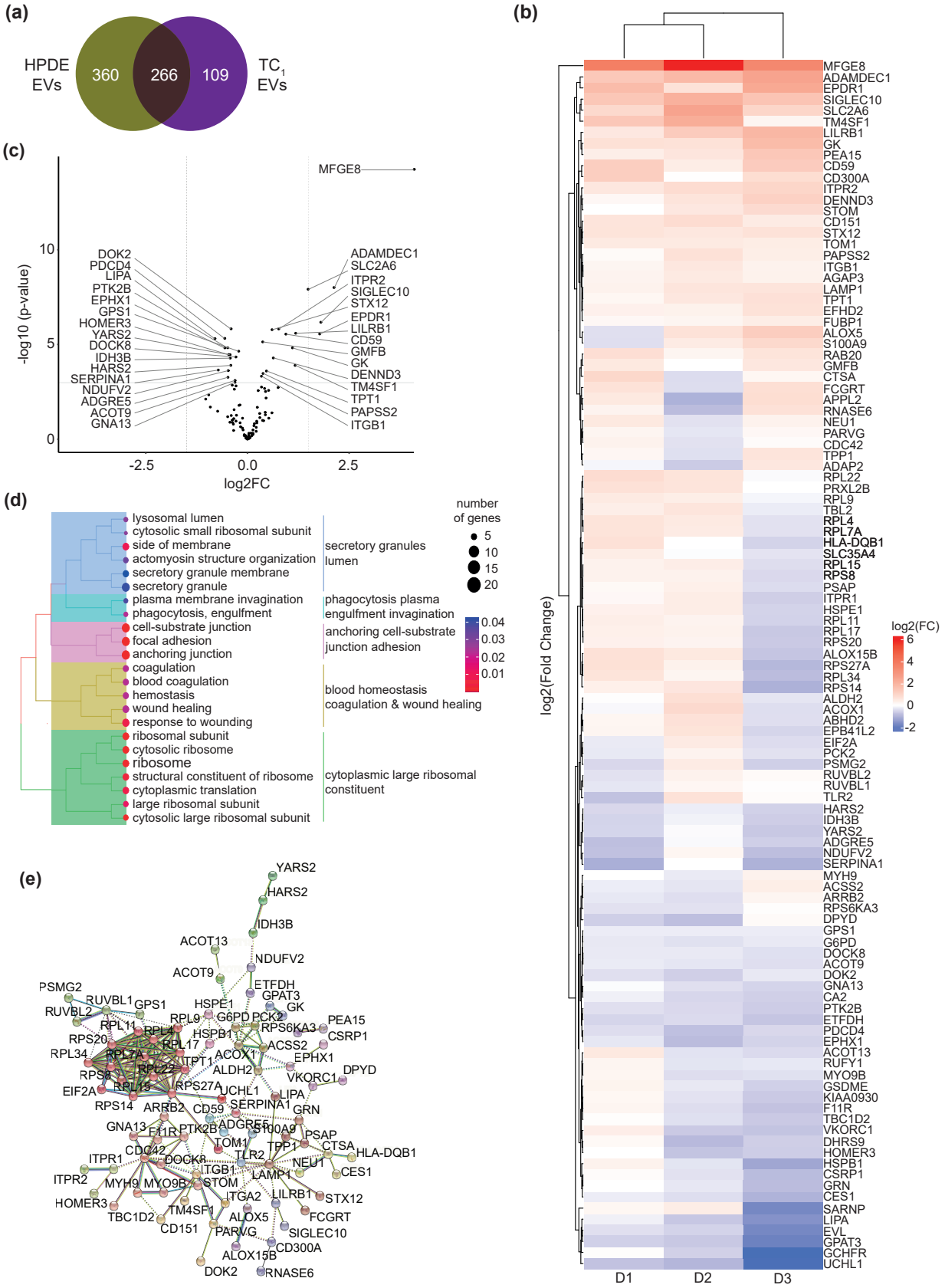

Figure 4. PDAC TC-EVs differentiated macrophages have a unique proteomic profile enriched with ribosome proteins and protein-synthesis pathways. (A) Venn-diagram comparing the number of differentially expressed proteins in TC_1-EVs differentiated macrophages with HPDE-EVs differentiated macrophages (N=3). **(B)** Heat map of significantly differentially expressed proteins in 3 healthy blood donor-derived monocytes differentiated by TC_1 EVs. **(C)** Volcano plot of significantly up- and down-regulated proteins in TC_1-EVs differentiated macrophages compared to untreated macrophages. **(D)** Overrepresentation analysis (ORA) tree plot of differentially expressed proteins in TC_1-EVs differentiated macrophages. **(E)** STRING protein interaction network of differentially expressed proteins in TC_1-EVs differentiated macrophages.

Figure 5.
Hussain et al.

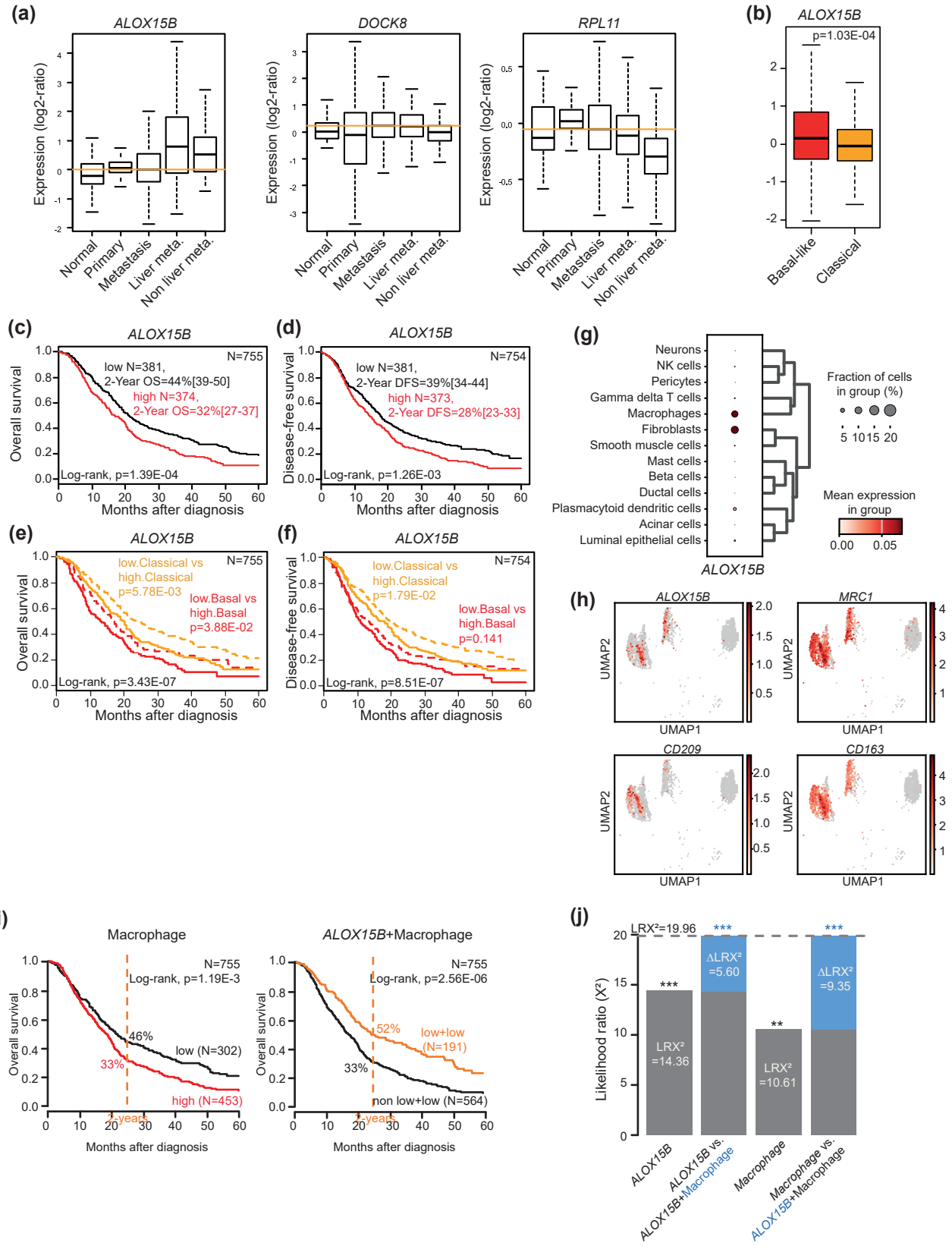

Figure 5. *ALOX15B* expression correlates with poor patient outcomes and is associated with M2-like macrophages in human PDAC. (A) Box plot of *ALOX15B*, *DOCK8* and *RPL11* mRNA expression (log2) as continuous values in PDAC primary samples (N=938), metastasis samples (N=152) and normal pancreatic samples (N=158). The orange line represents the median expression level across the whole cohort. **(B)** Box plot of *ALOX15B* mRNA expression (log2) in PDAC primary samples according to the molecular subtypes defined by Moffit et al. The p-value is for the t-test. **(C)** Kaplan-Meier curve of OS in PDAC patients according to *ALOX15B* expression, high or low. **(D)** Kaplan-Meier curve of DFS in PDAC patients according to *ALOX15B* expression, high or low. **(E)** Kaplan-Meier curve of OS in PDAC patients according to *ALOX15B* expression, high or low, and basal-like or classical Moffitt PDAC subtype. Low.Basal_Like N=110, 2-Year OS=32%[24-43], high.Basal_like N=152, 2-Year OS=25%[19-34]. Low.Classical N=271, 2-Year OS=50%[44-57], high.Classical N=222, 2-Year OS=36%[30-44]. **(F)** Kaplan-Meier curve of DFS in PDAC patients according to *ALOX15B* expression, high or low, and basal-like or classical Moffitt PDAC subtype. Low.Basal_Like N=110, 2-Year OS=27%[19-37], high.Basal_like N=151, 2-Year OS=20%[14-28]. Low.Classical N=271, 2-Year OS=44%[38-50], high.Classical N=222, 2-Year OS=33%[27-40]. **(G)** Dot plot results of *ALOX15B* in cell types from PDAC patients (GSE197177). **(H)** UMAP of leiden clusters and localization and expression of *ALOX15B*, and M2 markers (*CD206*, *CD209* and *CD163*) from PDAC patients (GSE197177). **(I)** Kaplan-Meier curve of OS in PDAC patients according to enrichment of macrophage scores, high or low (left), and according to *ALOX15B* expression combined with macrophage score, low *ALOX15B*-low macrophage score expression and non-low-*ALOX15B* or non-low macrophage score expression (right). **(J)** Comparison of prognostic information for OS of *ALOX15B* expression alone, macrophage score alone, and combination of *ALOX15B* expression and macrophage score in human PDAC patients using likelihood ratio analysis.

Figure 6.
Hussain et al.

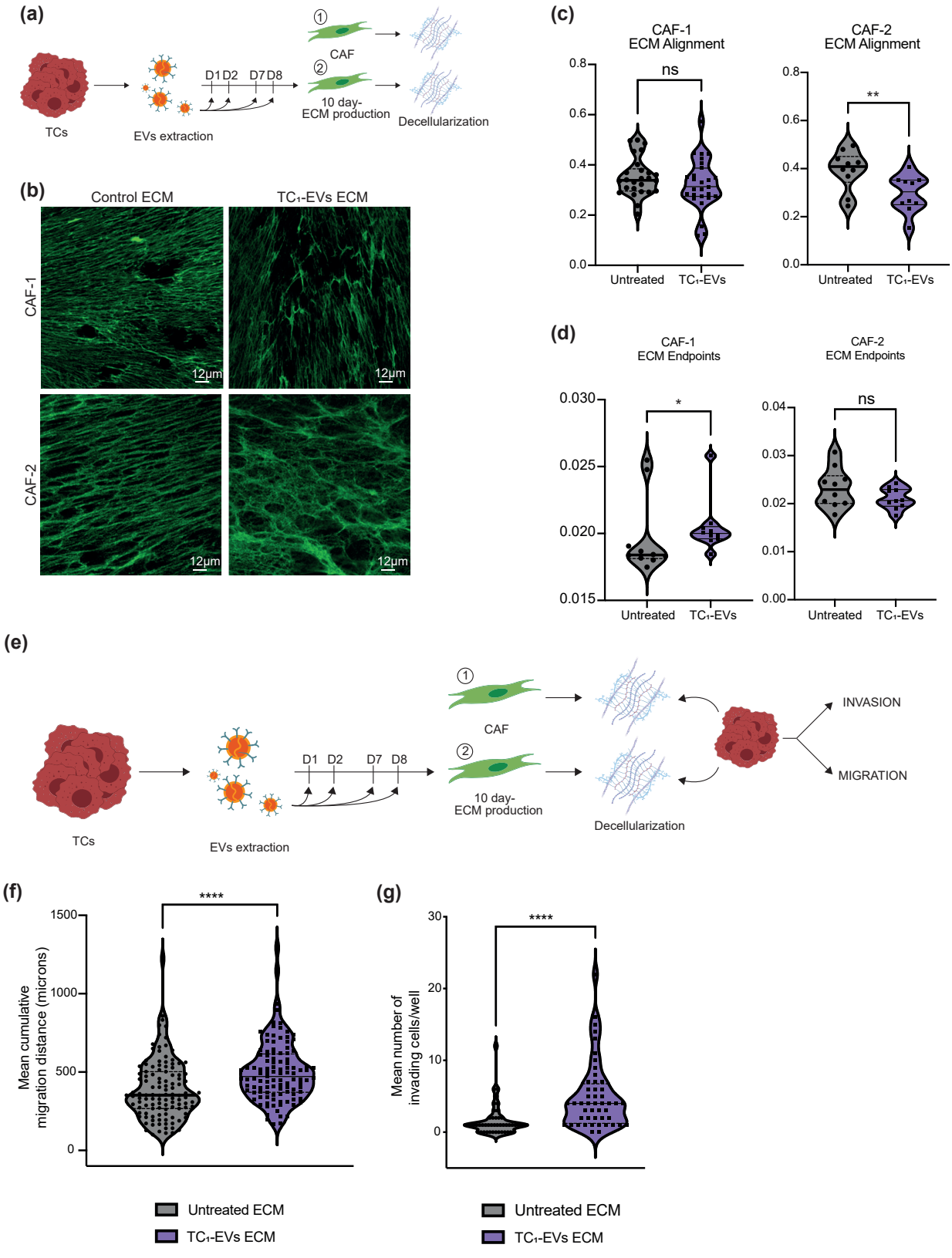

Figure 6. PDAC TC-EVs modify structural features of CAF-derived ECM and promote tumor cells aggressiveness. (A) Schematic depiction of experimental protocol: Primary CAFs were cultured for a period of 8 days during which they were treated four times, for two consecutive days, with TC-EVs. Following the culture period, ECMs were decellularized to remove CAFs and used for immunofluorescence staining or other functional studies. **(B)** Representative confocal microscopy images of fibronectin fibers (green) produced by untreated or TC_1-EVs treated primary CAFs derived from two different patients. Scale bars as indicated: 12µm. **(C)** Quantification of fibronectin fiber alignment by TWOMBLI of two primary CAFs-derived ECM (N=3). **(D)** Quantification of fibronectin fiber endpoints by TWOMBLI of two primary CAFs-derived ECM (N=3). **(E)** Schematic depiction of ECM production by CAFs as in Fig 6A followed by plating of tumor cells for migration and invasion assays. **(F)** Migratory capacity, in mean migration distance (microns), of TC_1 on ECMs produced by untreated or TC_1-EVs treated CAFs analyzed by time-lapse microscope over 12 hours (N=3). **(G)** Invasive capacity, in mean number of invading cells, of TC_1 on ECMs produced by untreated or TC_1-EVs treated CAFs through a Boyden chamber (8-micron pores) assay at 24 hours (N=3). Statistical analyses were performed using unpaired student's t-tests. Significant differences with p-values <0.0001 ****, <0.001 ***, <0.01 **, and <0.05 * are indicated.

Figure 7.
Hussain et al.

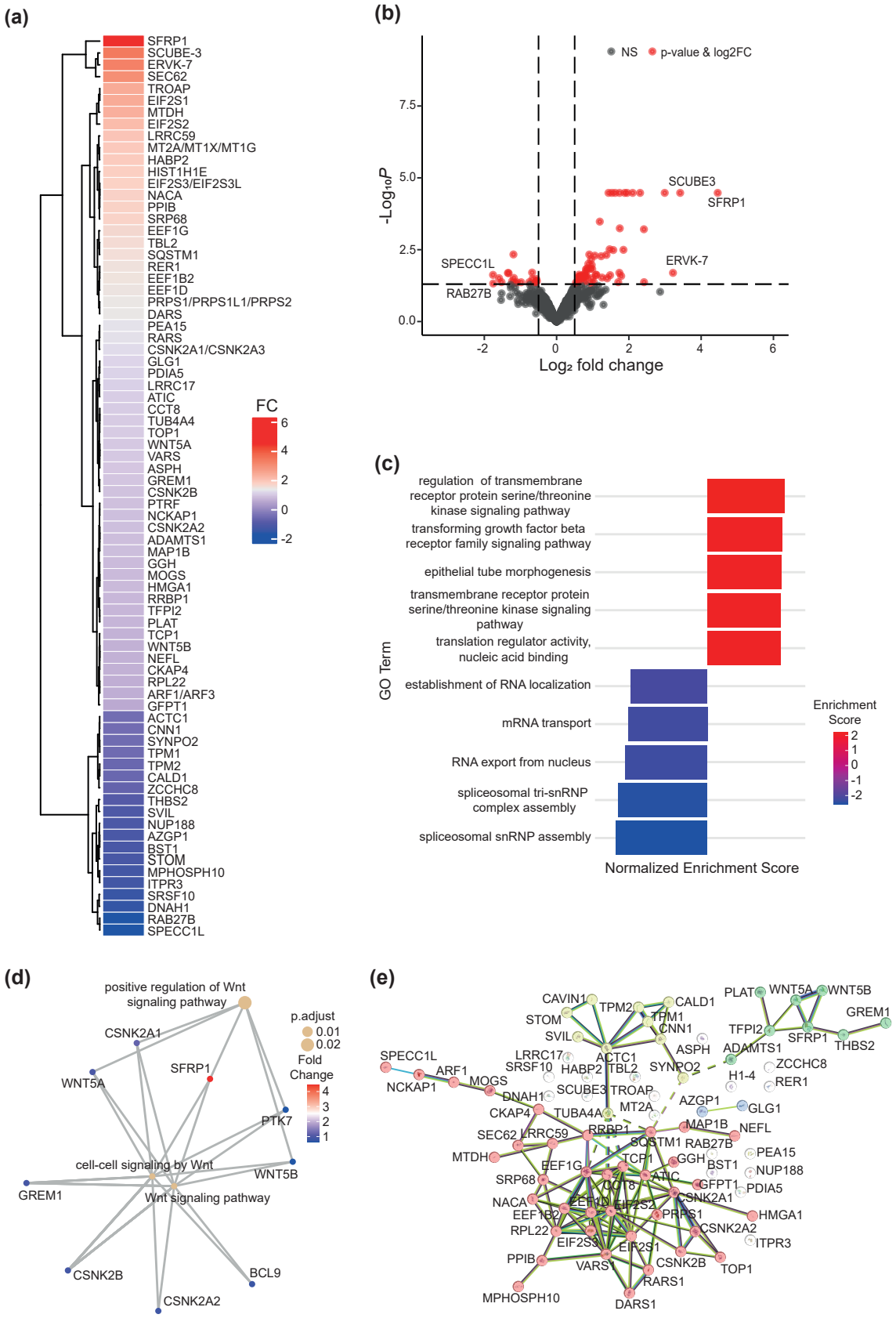

Figure 7. PDAC TC-EVs treated CAFs produce ECMs enriched in Wnt pathway proteins. **(A)** Heat map of mean log_2-fold changes of protein expression in CAF-derived ECMs treated with TC_1-EVs compared to untreated CAF-ECM (N=3). **(B)** Volcano plot of differentially expressed proteins in CAF-derived ECMs treated with TC_1-EVs compared to untreated CAF-ECM. **(C)** Gene ontology enrichment analysis depicting differentially expressed protein pathways in TC_1-EVs treated CAF-derived ECM. Terms associated with the proteins from the heatmap were selected and the top 10, including the five most upregulated and five most downregulated terms, were identified. **(D)** Network plot showing the relationship of SFRP1 and other genes in the Wnt signaling pathways and their relative fold changes between untreated and TC_1-EVs treated CAF-ECMs. **(E)** STRING protein network analysis of TC_1-EVs treated CAF-ECM.

Figure 8.
Hussain et al.

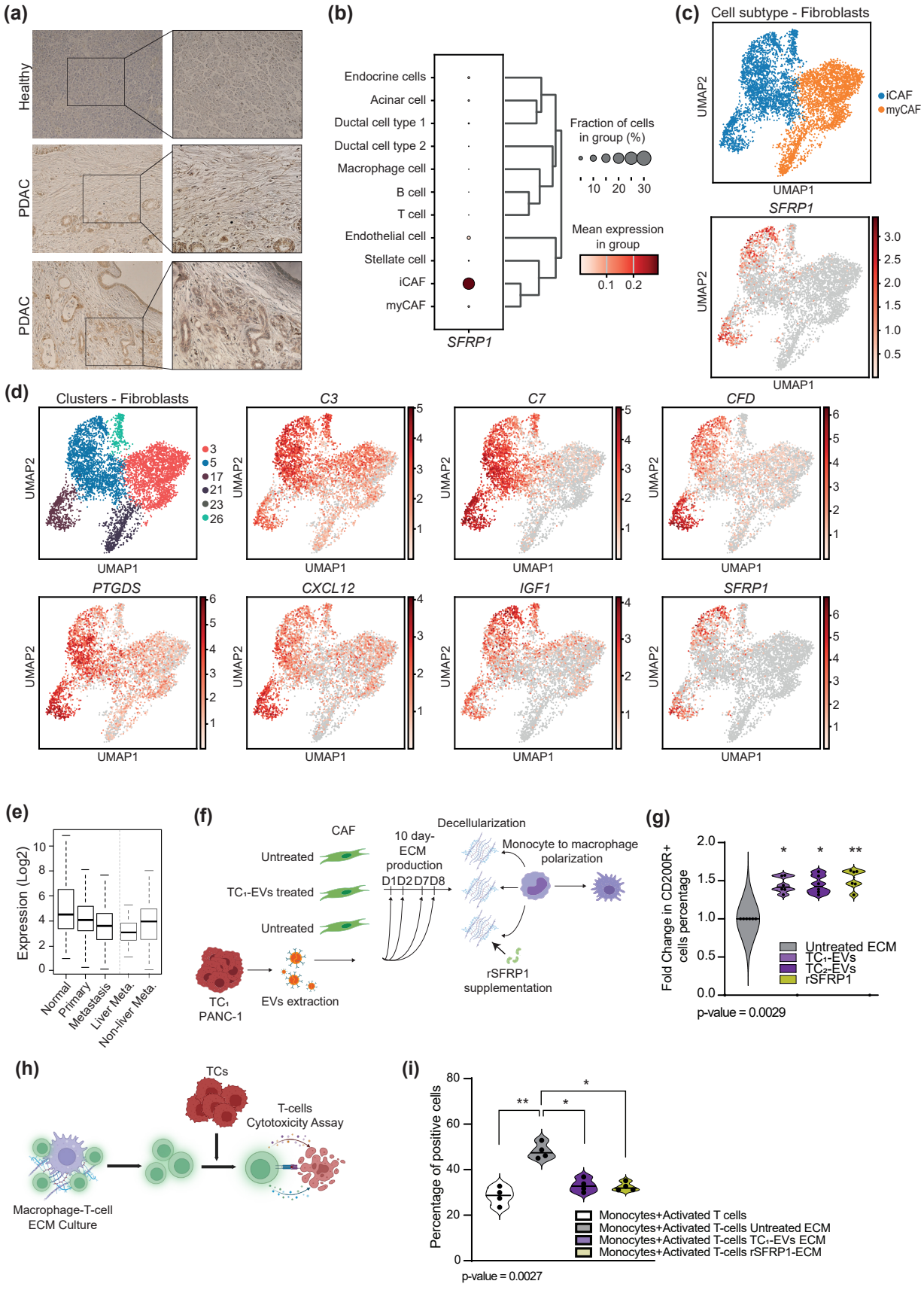

Figure 8. SFRP1 is expressed in a subset of inflammatory CAFs in human PDAC and suppress T-cell activity and cytotoxicity. (A) Immunohistochemical staining of SFRP1 expression in human healthy pancreas and PDAC tissue-microarrays. Images taken at 20x (left) and 40x (right) magnification. **(B)** Dot plot results of *SFRP1* in cell types from PDAC patients (CRA001160). **(C)** UMAP of CAFs subtypes and expression of *SFRP1*. **(D)** UMAP of leiden clusters of fibroblast cell types and expression of *SFRP1*, and iCAF markers (*C3*, *C7*, *CFD*, *PTGDS*, *CXCL12* and *IGF1*) in PDAC patients (CRA001160). **(E)** Box plot of *SFRP1* mRNA expression (log2) in PDAC primary samples (N = 938), metastasis samples (N=152) and normal pancreatic samples (N=158). **(F)** Schematic depiction of experimental protocol: Primary PDAC CAFs were cultured for ECM production as previously described and left either untreated or treated with TC_1-EVs. Following decellularization, healthy blood donor-derived monocytes were extracted as previously described and plated on decellularized ECM either without treatment or with treatment with recombinant SFRP1 (500ng/mL). **(G)** Fold change of $CD200R^+$ cell percentage on macrophages plated for 5 days on decellularized ECM derived from untreated CAFs, CAFs treated with TC_1-EVs, TC_2-EVs or rSFRP1 supplemented ECM (N=6, matched samples). **(H)** Schematic representation of experimental protocol: Same donor pan-T cells were added to macrophage-ECM cultures and incubated for 72h. T-cells were extracted from macrophage-T cell-ECM cocultures and cocultured with TCs for 72h followed by a T-cell mediated cytotoxicity assay (AnnexinV/PI staining). **(I)** Total percentage of cells positive for Annexin V or for propidium iodide (PI) and double positive for Annexin V/PI following 72h coculture with activated T-cells or activated T-cells cultured on decellularized ECM derived from untreated CAFs, CAFs treated with TC_1-EVs, and rSFRP1 supplemented ECM (N=4). Statistical analyses were performed using one-way non-parametric ANOVA Kruskal-Wallis test and Dunn's multiple comparisons tests (G and I). Significant differences with p-values <0.0001 ****, <0.001 ***, <0.01 **, and <0.05 * are indicated.

Table 1. List of antibodies and recombinant proteins

Antigen	Manufacturer	Reference	Fluorochrome
Alix	Abcam	ab117600	
Tsg101	Abcam	ab125011	
CD63	Abcam	ab271286	
CD81	Abcam	ab109201	
CD9	SantaCruz Biotechnology	SC-59140	
Syntenin	SantaCruz Biotechnology	SC-515538	
Fibronectin	SantaCruz Biotechnology	SC-8422	
SFRP1	ThermoFisher	PA5119647	
IBA1	ThermoFisher	PA5-18039	
CD206	Abcam	ab300621	
Sytox Green	ThermoFisher	R37168	FITC
Viobility	Miltenyi Biotec	130-110-207	405/520
CD14	Miltenyi Biotec	130-113-149	PE-Vio-770
CD14	Miltenyi Biotec	130-127-384	Vio-Bright-R720
CD16	Miltenyi Biotec	740098	BV421
CD16	Miltenyi Biotec	130-113-396	Vio-Blue
CD80	BD Biosciences	563315	BV605
CD83	BD Biosciences	565336	BV786
CD200R	Biolegend	329306	PE
CD200R	Miltenyi Biotec	130-111-291	APC
PDL1	Miltenyi Biotec	130-122-812	PE-Vio-770
HLADR	Biolegend	307618	APC-Cy7
HLADR	Miltenyi Biotec	130-111-792	APC-Vio-770
CD206	Biolegend	321142	BV-785
CD206	Biolegend	321105	PE
S100A9	Biolegend	350706	PE
CD4	Miltenyi Biotec	130-114-726	Vio-Bright-B515
CD8	Miltenyi Biotec	130-110-820	PerCP-Vio-700
CD25	Miltenyi Biotec	130-114-732	PE-Vio-770
CD28	Miltenyi Biotec	130-120-120	PE-Vio-615
CD69	Miltenyi Biotec	130-112-805	APC-Vio-770
CD107a	Miltenyi Biotec	130-111-847	APC
FoxP3	Miltenyi Biotec	130-125-579	PE
Annexin-V	Biolegend	640917	Pacific Blue
Propidium Iodide	Miltenyi Biotec	130-093-233	
rSFRP1	Biotechne	5396-SF-025	
rIL-2	Miltenyi Biotec	130-097-743	

Table 1. List of antibodies and recombinant proteins. Details include manufacturer, reference numbers and fluorochromes (for flow cytometry antibodies only).

Table 2. Pancreatic cancer data sets included in our analyses of correlation of gene expression and clinical features

Cohort Name	N	Normal true (N)	Peri-tumoral (N)	Primary (N)	Metastasis (N)
Badea	75	0	39	36	0
Chaika	75	0	0	15	60
Chen	63	0	0	63	0
Collisson	27	0	0	27	0
Grutzmann	25	11	0	11	3
ICGC_AU	96	0	0	96	0
ICGC_CA	211	0	0	195	16
Jamieson	53	0	8	45	0
Kirby	51	0	0	51	0
Moffit	107	46	0	0	61
Monzon	24	0	0	24	0
Park	11	5	0	6	0
Stratford	132	0	0	132	0
TCGA	155	0	4	150	1
vdBroeck	23	0	0	12	11
Winter	30	0	0	30	0
Zhang	90	0	45	45	0
Total	1248	62	96	938	152

Table 2. Pancreatic cancer data sets included in our analyses of correlations of gene expression and clinical features. A clinical cohort was compiled using 15 publicly available datasets from the National Center for Biotechnology Information (NCBI), GenBank GEO, ArrayExpress, EGA and TCGA databases that were generated from DNA microarrays (Affymetrix, Agilent) and RNA-sequencing (Illumina). The pooled dataset contained 1248 samples, including 938 primary PC samples, 152 metastasis samples, and 158 normal pancreatic samples.

Table 3. Commonly deregulated genes in TC-1 and TC-2 EVs treated macrophages

Gene	(-)Log Student's T-test p-			Student's T-test q-value			Student's T-test Difference		
TC-1 EVs	D1	D2	D3	D1	D2	D3	D1	D2	D3
ALOX15B	3.8543	3.1069	5.7230	0.1920	0.2413	0.2445	0.2828	0.4021	-0.1995
ABHD2	3.8713	1.6034	3.1045	0.1385	0.4288	0.2400	0.3821	0.1175	-0.2131
ALDH2	5.6494	0.2302	3.6522	0.1194	0.7987	0.2880	0.4127	0.0246	-0.1644
CTSA	4.0416	5.2211	0.7229	0.2223	0.1673	0.4043	-0.2285	0.5458	0.1097
DOCK8	4.3633	2.8585	4.3438	0.3072	0.4021	0.2462	-0.1246	-0.1297	-0.2007
DOCK2	8.6743	0.3369	5.7230	0.1300	0.7156	0.2445	-0.3693	-0.0378	-0.1995
LAMP1	4.0310	3.3333	4.1212	0.1645	0.3671	0.1510	0.3258	0.1554	0.3371
PAPSS2	6.9286	0.8379	3.4755	0.1354	0.5563	0.2499	0.3670	0.0700	0.1978
RP11	2.7151	3.6334	3.3122	0.2802	0.3356	0.1726	0.1489	0.1896	-0.3049
RPL15	3.0398	2.8149	3.7888	0.2331	0.3704	0.2376	0.2066	0.1528	-0.2129
RPL9	3.0018	4.7359	0.2047	0.2357	0.2774	0.5723	0.2019	0.2607	-0.068
TPT1	3.1301	0.9958	5.2207	0.1863	0.4484	0.1245	0.2986	0.1087	0.3828
TC-2 EVs	D1	D2	D3	D1	D2	D3	D1	D2	D3
ALOX15B	3.1504	1.1507	3.6554	0.4964	0.1348	0.3386	0.2053	0.3403	0.5131
ABHD2	1.9633	4.6254	3.5031	0.4953	0.0612	0.4659	0.2213	0.4360	0.3143
ALDH2	4.1605	4.6372	2.6208	0.4910	0.2181	0.4848	0.2924	0.1827	0.2374
CTSA	3.6477	0.3340	3.1062	0.4969	0.4617	0.4378	-0.2033	-0.0851	0.3693
DOCK8	3.0302	3.6999	2.7952	0.5855	0.2872	0.5238	-0.0814	-0.1316	-0.1398
DOCK2	5.7290	4.1607	0.3650	0.4987	0.2440	0.7683	-0.1562	-0.1597	-0.0510
LAMP1	1.8348	5.4369	4.1337	0.5058	0.0816	0.5121	0.1554	0.3666	0.1586
PAPSS2	4.0036	4.0273	1.9034	0.5108	0.2092	0.5229	0.2581	0.1944	0.1483
RP11	1.1768	3.1180	3.1014	0.5520	0.2130	0.5234	0.1064	0.1936	0.1389
RPL15	3.0887	5.4372	1.8222	0.4968	0.1241	0.5274	0.2060	0.2830	0.1352
RPL9	2.1295	3.7383	3.1215	0.5060	0.0542	0.4868	0.1514	0.4971	0.2138
TPT1	3.0881	6.9128	1.7899	0.4942	0.0340	0.4849	0.2131	0.6029	0.2356

Table 3. Commonly deregulated genes in TC_1- and TC_2-EVs treated macrophages. Differential expression analyses were performed on proteomic profiles of TC_1- and TC_2-EVs treated macrophages from three different healthy donors and the 12 significantly commonly deregulated genes were selected ((-) log p-values cut off values ≥3 in at least two out of three donors to account for inter-donor heterogeneity).

Table 4. Differentially expressed genes accross cell subtypes of Macrophages

clusters	markers	scores	logfoldchanges	pvals	pvals_adj	cell type
4	MRC1	14.62	2.69	2.06E-48	7.73E-47	Macrophage cells
4	CD163	13.34	2.27	1.43E-40	4.112E-39	Macrophage cells
4	CD83	11.92	1.36	9.41E-33	2.10E-31	Macrophage cells
4	ALOX15B	2.64	2.16	0.01	0.02	Macrophage cells
4	CD74	2.57	0.66	0.01	0.03	Macrophage cells
4	CD209	0.47	1.09	0.64	0.93	Macrophage cells
10	CD74	44.36	5.22	0	0	Macrophage cells
10	MRC1	41.73	6.29	0	0	Macrophage cells
10	CD163	41.45	6.08	0	0	Macrophage cells
10	CD83	28.22	3.66	2.93E-175	3.75E-173	Macrophage cells
10	CD209	11.68	6.91	1.55E-31	2.48E-30	Macrophage cells
10	ALOX15B	4.20	2.89	0.01	0.01	Macrophage cells
11	CD74	52.54	4.05	0	0	Macrophage cells
11	CD163	45.51	5.42	0	0	Macrophage cells
11	CD83	42.41	3.81	0	0	Macrophage cells
11	MRC1	41.51	5.05	0	0	Macrophage cells
11	ALOX15B	6.43	3.12	1.29E-10	7.13E-10	Macrophage cells
11	CD209	2.59	2.78	0.01	0.03	Macrophage cells

Table 4. Differentially expressed genes across cell subtypes of macrophages in human PDAC. Differential expression scores, log-fold changes, and p-values for M1- and M2-macrophage marker genes and ALOX15B in PDAC patient single-cell RNA sequencing dataset as seen in Figure 5J and S6F (GSE197177).

Table 5. Differentially expressed genes accross cell subtypes of Fibroblasts

clusters	markers name	scores	logfoldchanges	pvals	pvals_adj	cell subtype
3	C3	25.92	1.43	1.33E-131	2.87E-130	myCAF
3	PTGDS	20.67	1.46	6.26E-88	9.11E-87	myCAF
3	CXCL12	11.99	0.82	2.55E-32	1.69E-31	myCAF
3	IGF1	11.69	1.23	8.56E-31	5.52E-30	myCAF
3	CFD	-2.85	-0.18	0.01	0.01	myCAF
3	SFRP1	-12.19	-1.89	1.07E-33	7.30E-33	myCAF
3	C7	-14.83	-0.98	2.55E-48	2.25E-47	myCAF
5	C7	77.10	5.09	0	0	iCAF
5	C3	61.31	3.61	0	0	iCAF
5	PTGDS	48.02	4.15	0	0	iCAF
5	IGF1	34.44	4.36	7.06E-209	4.29E-207	iCAF
5	CXCL12	30.07	2.12	2.34E-168	1.04E-166	iCAF
5	CFD	28.50	2.51	2.95E-153	1.15E-151	iCAF
5	SFRP1	18.39	3.66	2.08E-70	3.18E-69	iCAF
17	C7	111.812	6.55	0	0	iCAF
17	PTGDS	65.12	6.43	0	0	iCAF
17	CXCL12	54.53	4.55	1.46E-269	1.41E-267	iCAF
17	CFD	42.78	6.24	2.06E-206	1.38E-204	iCAF
17	IGF1	26.06	4.13	3.45E-108	1.04E-106	iCAF
17	C3	25.02	2.27	2.63E-102	7.38E-101	iCAF
17	SFRP1	16.87	4.489	1.17E-54	1.69E-53	iCAF
21	PTGDS	7.94	0.96	9.48E-15	5.49E-14	myCAF
21	C3	1.92	0.16	0.06	0.09	myCAF
21	SFRP1	-0.41	-0.14	0.68	0.75	myCAF
21	CFD	-6.41	-0.77	2.71E-10	1.19E-09	myCAF
21	CXCL12	-7.31	-0.89	7.48E-13	3.88E-12	myCAF
21	IGF1	-14.29	-2.42	1.70E-41	2.63E-40	myCAF
21	C7	-17.82	-1.98	1.59E-59	3.87E-58	myCAF
26	C3	22.03	3.28	3.92E-61	1.31E-59	iCAF
26	IGF1	15.86	4.22	6.54E-40	1.18E-38	iCAF
26	C7	13.14	2.69	1.56E-30	2.04E-29	iCAF
26	CXCL12	9.27	1.78	7.42E-18	5.49E-17	iCAF
26	SFRP1	4.90	2.33	1.73E-06	5.66E-06	iCAF
26	PTGDS	4.45	0.96	0.01	0.01	iCAF
26	CFD	-1.57	-0.37	0.12	0.17	iCAF

Table 5. Differentially expressed genes across cell subtypes of fibroblasts in human PDAC. Differential expression scores, log-fold changes, and p-values for myCAF, iCAF, and apCAF marker genes and SFRP1 in PDAC patient single-cell RNA sequencing dataset as seen in Figure 8D and S8A (CRA001160).

Table 6. Differential Clinical Characteristics between SFRP1 high and low groups

		SFRP1			
Characteristics	**N**	**low**	**high**	**p-value**	**statistic**
N				0.0522	3.8
0	136	75 (35%)	61 (26%)		
1	307	137 (65%)	170 (74%)		
Taube_EMTMetaG_Score	923	-0.26 (-2.39-3.08)	0.21 (-1.66-2.14)	4.89E-28	-11
Bailey classification				2.53E-12	57
ADEX	179	62 (13%)	117 (25%)		
Immunogenic	156	79 (17%)	77 (17%)		
Pancreatic_Progenitor	258	176 (38%)	82 (18%)		
Squamous	330	143 (31%)	187 (40%)		
Collisson classification				7.57E-13	56
Centroid_Classical.PDA	427	267 (58%)	160 (35%)		
Centroid_Exocrine.like.PDA	262	90 (20%)	172 (37%)		
Centroid_QM.PDA	234	103 (22%)	131 (28%)		
Moffitt_NMF_type				1.13E-02	6.4
Basal_like	331	146 (32%)	185 (40%)		
Classical	592	314 (68%)	278 (60%)		
Bindea_Macrophages	923	-0.01 (-1.8-1.34)	0.18 (-1.42-1.88)	3.97E-10	-6.3

Table 6. Differential clinical characteristics between SFRP1 high and low groups in PDAC patient cohort. Percentage of patients with annotated clinical characteristics (node, EMT score, tumor subtypes, and macrophage cell scores) associated with high or low SFRP1 expression.